

REVISION 1

Ilmenite breakdown and rutile - titanite stability in metagranitoids:

natural observations and experimental results

Samuel Angiboust^(1,2) and Daniel Harlov⁽¹⁾

(1) Deutsches GeoForschungsZentrum, Telegrafenberg, D-14473 Potsdam, Germany. (dharlov@gfz-potsdam.de)

(2) Institut de Physique du Globe de Paris, Sorbonne Paris Cité, Univ. Paris Diderot, CNRS, F-75005 Paris, France (*: corresponding autor) samuel.angiboust@gmail.com

ABSTRACT

Rutile and titanite commonly form by replacement of ilmenite in metamorphic rocks. Exhumed orthogneiss from the W. Alps show that titanite is mostly stable below 1 GPa while rutile seems to dominate within rocks recrystallized under higher pressures. We herein investigate phase relationships for four granitic compositions with variable CaO content at medium to high-pressure conditions (0.7-1.6 GPa, 450-650°C) with a focus on ilmenite breakdown and Ti-bearing species formation. Our piston-cylinder experiments show that, in the investigated P-T range, ilmenite reacts during metamorphism above 1.2-1.4 GPa to form rutile. Below this pressure, titanite is the dominant Ti-bearing species for most granitoid compositions. We also show that the position of this reaction curve is strongly influenced by the whole rock Ca activity. For low Ca activities, rutile may be stable down to 0.7 GPa (and below) within ilmenite pseudomorphs while the titanite

stability field may extend to pressures >1.3 GPa for Ca-richer compositions. Both species may be co-stable in one single sample depending on the local Ca activity gradients. The finding of metamorphic rutile within metagranitoids with CaO contents >2 wt% can be considered, under certain conditions, as a reliable indicator of high-pressure metamorphism. This study also highlights the importance of improving our knowledge of the phase relationships between rutile and titanite as a function of P-T-X in order to better interpret the textural and tectonic history in natural samples as well as the meaning of age values yielded by rutile and titanite geochronometers.

Keywords

rutile, titanite, ilmenite, experimental petrology, metamorphic petrology, granite

INTRODUCTION

Metamorphosed granites are a common rock type in former convergent settings where high-pressure (HP) rocks are exhumed (e.g. Proyer 2003; Massonne 2015). Evaluating the pressure-temperature history of meta-acidic systems is notably more difficult than for basic lithologies where high-pressure recrystallization proceeds more efficiently and where mineral assemblages are more suited for thermobarometric purposes. In the absence of sodic clinopyroxene, silica substitution in phengite crystals is commonly used as a geobarometer to estimate the pressure in metagranitic rocks (e.g. Evans and Patrick 1987; Angiboust et al. 2014). The presence of rutile [TiO₂] is sometimes used as an argument to support the former existence of a high-pressure stage in such rocks (e.g. Gaggero et al. 2009). Titanite [CaTiSiO₅] rims around rutile or ilmenite [FeTiO₃] are generally interpreted as products of rutile re-equilibration during exhumation (Carswell

and O'Brien 1993; Harlov et al. 2006; Lucassen et al. 2011; Pearce and Wheeler 2014). However, the actual location of rutile and titanite-forming reactions in P-T-X space remain poorly constrained.

Liou et al. (1998) studied the stability of titanite, rutile, and ilmenite in a basaltic system between 600 – 1000°C and up to 3 GPa. These authors found that rutile has a slightly positive reaction slope and is stable above 1.4 – 1.6 GPa in this temperature range. Below this curve, titanite is the stable phase in the range 0.3 – 1.2 GPa and 600 – 700°C and ilmenite stable above 700 – 750°C over the same pressure range. However, the stability of these minerals is probably buffered by the existence of other mineral species and by the presence of elements such as Ca and Na (Liou et al. 1998). In particular, the whole rock Ca budget may significantly change the stability field of Ti-bearing minerals as Ca enters the titanite structure as a major element. As a consequence, the titanite stability field may expand towards higher pressures for Ca-rich systems (Frost et al. 2001).

Titanite and rutile have been increasingly used as geothermometers and geospeedometers over the last 15 years in order to understand the pressure-temperature-time (P-T-t) trajectories of metamorphic rocks in collisional settings (Frost et al. 2001; Zack et al. 2004; Kylander-Clark et al. 2008; Tropper & Manning, 2008; Smye and Stockli 2014; Gasser et al. 2015). Despite the importance of these accessory minerals in solving geodynamic issues, experimental constraints on rutile-titanite-ilmenite phase relationships as a function of P-T- X_{Ca} are lacking for metagranitic and metasedimentary systems (e.g. Luvizotto et al. 2009; Meinhold 2010).

In this study we document natural rutile-titanite-ilmenite reaction textures in granitoid rocks buried and exhumed during regional metamorphism in the Western Alps. In response to these natural observations, we performed a series of 11 piston-cylinder runs

consisting of four experiments per run for a series of four whole rock granitic to granodioritic compositions in order to (i) better localize phase transitions for rutile and titanite in the range 450-650°C / 0.7–1.6 GPa (corresponding to depths of approximately 25 to 50 km), and (ii) understand the effect of changing Ca activity in granitoid rocks on phase relationships in the Ti-NCKFMASH system.

OBSERVATIONS FROM NATURAL SAMPLES

Petrological observations from Western Alps

The Western Alps belt exhibits fragments of the European continental margin subducted and subsequently exhumed from various depths between the late Cretaceous and late Eocene (Tricart 1984; Dal Piaz et al. 2001). This belt, therefore, provides a good natural laboratory to assess the stability of rutile or titanite for upper continental crust compositions. The P-T range encompassed by the exhumed granitic slivers ranges from greenschist-facies (e.g. Mont Blanc massif) to eclogite-facies (e.g. Sesia zone, Dora Maira). **Table 1** summarizes reports of rutile and titanite occurrences and associated peak metamorphism P-T conditions for a broad range of metagranitoid bodies along the Alpine belt between Switzerland, Italy, and France. This table shows that titanite is generally stable at pressures below 1 GPa. Above 1.2 GPa, rutile becomes largely prevalent even though titanite may occasionally persist in eclogite-facies granitic rocks (Lombardo et al. 1977). In most localities, where rutile formed during peak burial conditions, rutile is surrounded by titanite indicating the partial reversion of rutile to titanite during exhumation.

Microstructural observations from the Arolla Gneiss

The Arolla gneiss, which outcrops at the base of the Austroalpine Dent Blanche massif, consists of a variety of felsic orthogneiss compositions ranging from monzogranites to granodiorites (Roda and Zucali 2011; **Table 2**). Petrological investigations of the Arolla orthogneiss revealed the existence of an upper greenschist-facies to lower blueschist paragenesis made up of albite, quartz, phengite, chlorite, epidote, tremolite, pyrite, rutile (rimmed by titanite), and occasionally Mg-riebeckite and aegyrine-augite (Pennacchioni and Guermani 1993; Angiboust et al. 2014; **Fig. 1a**). Recent thermobarometric estimates have shown that this tectonic slice has been coherently subducted during Alpine metamorphism down to 1.3 GPa and 450 to 500°C (Angiboust et al. 2014). These rocks are interesting for the purpose of our study because (rare) ilmenite remnants have been observed within rutile-titanite aggregates (**Fig. 1b**). Where preserved, the ilmenite is only visible as skeleton-like shapes and commonly exhibits evidence of strong dissolution (**Fig. 1b,c**). Replacement by rutile apparently took place along a crystallographic network within the ilmenite. One sample exhibits a crack within an ilmenite crystal healed by numerous, small rutile crystals, suggesting that replacement after micro-fracturing took place within the rutile stability field (**Fig. 1d**). In this unit, the thickness of the titanite rim around the rutile cores clearly correlates with the intensity of the greenschist-facies retrograde overprint. In the most retrogressed domains, the Arolla orthogneiss samples exhibit 20 to 50 μm wide titanite ribbons in which the prograde to peak metamorphic history (namely the rutile-bearing pseudomorphs after ilmenite) has been completely erased during exhumation.

EXPERIMENTAL PROCEDURE AND ANALYTICAL CONDITIONS

Granitoid glasses

The granitoid starting material used comes from a set of four granitoids collected in the Dent Blanche massif (Arolla orthogneiss; Angiboust et al. 2014) of the Western Alps. This set of coarse-grained granitoid rocks were selected because (i) they exhibit only minor alpine deformation with no visible evidence for fluid-rock interaction, (ii) they constitute a representative sampling of Arolla gneiss lithologies, and (iii) they exhibit a range of Ca contents ranging from 0.9 wt% to 3.2 wt% CaO (**Table 2**). The analytical procedure for X-ray fluorescence analysis of bulk-rock Arolla granitoid compositions (**Table 2**) is given in Angiboust et al. (2015). The starting granitic material is devoid of graphite and carbonate. The CaO content range considered here (0.9-3.2 wt%) encompasses most granitic compositions worldwide (average granitic composition: 1.85 wt% CaO; Le Maitre 1976; **Fig. 2a and 2b**). These compositions also share many similarities with greywacke compositions (e.g. Auzanneau et al. 2006; **Fig. 2b**).

Two kilograms of each granitoid sample were finely crushed and fifty grams of this powder were thoroughly milled in an agate mortar in ethanol and then dried at 100 °C. The dry granitic powder was then placed in a Pt crucible with a loose-fitting lid and melted at 1300 °C for four hours exposed to air. The melt was then quenched to a glass by dropping the Pt crucible in a litre of distilled water. Twenty grams of each granitoid glass were thoroughly milled in an agate mortar in ethanol. The bulk composition of each of the four glasses is given in **Table 3**. The slight discrepancy in the SiO₂ content between major element compositions for samples GR1 to GR3 (Tables 2 and 3) may derive from the presence of small quartz crystals that have been observed under SEM imaging in the analysed glass material. The formation of these crystals (possibly during the quenching stage or due to incomplete melting of the initial powder) likely led to a minor depletion of silica in the glass. Given that the system is already saturated in silica, it is highly unlikely that they had any effect on the phase relationships described here.

Experiments

In order to reproduce a natural granitic system and to identify overgrowth textures forming at various P-T conditions, we first created a mixture of natural, chemically homogeneous, 50 – 200 μm size mineral grains composed of 25% ilmenite (Bohemian Massif), 25% hornblende (Eifel mountains, Germany), 25% allanite (Jotunheimen pegmatite, Norway), and 25% muscovite (pegmatite, southern Norway). These mineral grains served as nuclei to visualize and understand the mineral phase relationships over the P-T space covered by our experiments. Given that the reaction volume at these low temperatures is limited to the surrounding of the mineral seed, the relatively high amount of mineral seeds does not modify the phase relationships studied here. Each experiment was prepared by loading 5 mg of doubly distilled pure water, 7 mg of the mineral mix, 13 mg of granitoid glass, and c. 1 mg of NaS into a 3 mm diameter, 1 cm long Au capsule. NaS was added in order to reproduce pyrite-pyrrhotite textures commonly observed in the Arolla orthogneiss. In the experiment, the mineral grains represent 33% of the total solid mass. Introduction of such a relatively large amount of mineral seeds in the glass matrix is needed to increase the chances of observing reaction textures during the evaluation of experimental results. Given the very sluggish reaction rates in the temperature window studied here (450 – 650°C; see experimental textures below), it is assumed that the introduction of these mineral seeds does not modify the overall effective composition of the matrix glass. In other words, there is no petrological, mineralogical, or geochemical evidence that the reaction volume around each mineral seed is influenced by the presence of the other seeds disseminated throughout the granitic glass. Each crystal seed reacts within the glass matrix surrounding it independent of the amount or the composition of the other seeds in the same system

(i.e. in the same Au capsule). In other words, the reactive bulk composition is controlled here since the seed surface corresponds to the locus where the replacement reaction will proceed at the contact with the surrounding granitic glass. Very local, Ca-richer zones may be created in the neighbourhood of reacting allanite and hornblende seeds but not in the case of the ilmenite or muscovite seeds, as surely would be the case in natural granitoid samples recrystallizing during metamorphism (see discussion section). The Au capsules were arc-welded shut using an argon plasma torch. The Au capsule seals were checked for leaks by first weighing, then being placed in a 105°C oven for 4 hours, and then weighing again. Only those capsules, which showed no loss in weight, were used in the experiments. The experiments utilized in this study are summarized in **Table 4**.

Experiments were performed using a Johannes design piston-cylinder apparatus (Johannes et al. 1971; Johannes 1973) and a NaCl assembly (pressure medium) with a cylindrical graphite oven. Four gently flattened Au capsules, separated by biotite sheets, were positioned vertically with the Ni-Cr thermocouple tip placed approximately halfway up along side of one of the Au capsules in order to prevent them from welding together during the course of the experiment (cf. **Fig. 3**). Temperatures are around 15 °C lower at the capsule tip compared to the capsule centre at 650 °C for the 650 °C experiments, 10 °C for the 550 °C experiments, and 5 °C for the 450 °C experiments. Biotite sheets were used to separate the capsules. At the start of a run, the pressure was taken up to approximately 10 to 15% below the run conditions, and then the temperature was brought up to the desired value. Thermal expansion caused the pressure to increase to the approximate target value. The pressure was then adjusted to the desired value, and automatically maintained within a preset range (+/- 50 MPa) during the course of the experiment. During the run, the presence of the graphite oven buffered the experiment to the C-CO-CO₂ oxygen buffer. Experiments were run over a variable amount of time from

11 to 56 days. Quench was achieved by turning off the current, such that H₂O-cooling jacket cooled down the NaCl assembly to below 50°C within about 15 sec.

After quench, the capsules were cleaned, weighed, opened, and dried in open air in a 100°C oven for 3 to 4 hours. They were weighed again in order to determine the exact fluid content (**Table 4**). The dried mineral mix was then extracted from the Au capsule, mounted in epoxy grain mounts, and then finely polished.

Scanning electron microscopy (SEM) and electron microprobe (EMP) analysis

Carbon coated grain mounts were first evaluated using high contrast back scattered (BSE) imaging on a Zeiss DSM-962 Scanning Electron Microscope at the Deutsches GeoForschungsZentrum, Potsdam, with an accelerating voltage of 20 kV and a focused electron beam.

Electron microprobe (EMP) compositional analyses were made using a JEOL Hyperprobe JXA-8500F with a field-emission cathode and five wavelength dispersive spectrometers at the Deutsches GeoForschungsZentrum Potsdam. Standards used for the calibration were the following: orthoclase (Al, Si, K), fluorite (F), rutile (Ti), Cr₂O₃ (Cr), wollastonite (Ca), tugtupite (Cl), albite (Na), MgO (Mg), Fe₂O₃ (Fe), and rhodonite (Mn). For most minerals, spot analyses for minerals (with a 1 µm beam) were done using a 15 kV accelerating voltage and 10 nA beam current. EMP evaluation of granitoid glasses were done using a 20 kV accelerating voltage, a 2 nA beam current, a 10 µm beam diameter and counting time of 5 seconds of Na and Si and 10 seconds for the other elements. For REE-bearing minerals (titanite, epidote and allanite), a beam current of 40 nA and a 1 µm beam diameter with a 60s counting time for each element was used. Natural and synthetic minerals were used as calibration standards. Due to the extremely

small size of the analysed crystals and the presence of fine-grained intergrowths, only few analyses yielded correct element proportions and totals. Starting material compositions are given in **Table 3** and representative mineral product analyses are available in **Table 5**. Mineral abbreviations used throughout this work are from Whitney and Evans (2010).

EXPERIMENTAL RESULTS

Experiments at 650 °C

Four sets of four experiments were run at 650 °C for a set of pressures between 0.8 and 1.6 GPa. Representative BSE images of textures are presented in **Figure 4** (see also **Table 4**). At 1.3 GPa and 1.6 GPa, rutile is ubiquitous, replacing ilmenite along cracks and cleavages (**Fig. 4a**). Titanite was not observed within the ilmenite pseudomorphs nor in the recrystallized matrix. At 1.6 GPa, the original hornblende seeds are overgrown by an aegyrine-rich clinopyroxene (**Fig. 4b**; **Table 5**) and plagioclase is not visible in the matrix. Newly formed quartz grains are visible in the matrix associated with sub-micron needles of clinopyroxene. At 1.3 GPa, hornblende seeds are rimmed by Fe-enriched hornblende (#64; **Table 4**). Biotite is typically observed as a replacement product associated with rutile within and around ilmenite pseudomorphs (**Fig. 4c**). At 1.0 and 1.3 GPa, a glass is observed within the ilmenite pseudomorphs, mixed with rounded remnant grains of ilmenite (**Fig. 4d**). Some of these textures have been described in similarly altered ilmenite grains forming under relatively low temperature conditions although at higher oxidation states (cf. Melcher, 1991). The composition of this glass is close to granitic but different from the starting material (**Table 5**). At 1.0 GPa, while rutile is the dominant Ti-bearing phase in the experiment, local small aggregates of titanite are

visible in the matrix derived from the two granitoid glasses with the highest Ca contents (**Table 4**). EMP analysis of a titanite crystal surrounding an allanite yielded an REE concentration of c. 1.1 wt.% (**Table 5**), which reflects REE contents commonly found in natural titanites (cf. Harlov et al., 2006). At 0.8 GPa, titanite is the dominant Ti-bearing phase in all four experiments (**Table 4**). It forms numerous c. 5 μm long lozenges within the recrystallized matrix (**Fig. 4e**). At 0.8 GPa, rutile is only visible as rare, μm -sized fringes replacing ilmenite in the matrix with the lowest Ca content (GR1 and GR2; **Table 4**).

Amphibolite-facies assemblages, consisting of biotite, epidote, plagioclase, and hornblende, are visible between 0.8 and 1.3 GPa. Epidote is stable over the entire pressure range investigated here, rimming allanite but also spatially associated with titanite when present (**Fig. 4f**). Epidote locally contains a significant amount of REE (ca. 10 wt% based on EDS analyses at the SEM). Biotite is stable over the entire pressure range (0.8-1.6 GPa), forming 10 to 100 μm flakes randomly distributed in the recrystallized matrix and within pseudomorphs after ilmenite and hornblende (**Table 5**). Initial muscovite seeds have been completely transformed to biotite over the entire pressure range. Pyrite (or pyrrhotite) forms as 1-5 μm crystals in the vicinity of ilmenite pseudomorphs or in the recrystallized matrix.

Experiments at 550 °C

Four sets of four experiments were run at 550°C for pressures between 0.7 and 1.3 GPa (**Fig. 5; Table 4**). Here, the resulting amphibolite-facies assemblages were slightly different than the ones obtained at 650 °C. Experiments #41–#44 at 1.3 GPa indicate that rutile is the only stable Ti-rich phase to form from ilmenite and that titanite is

completely absent from the sample (**Figs. 5a and 5b**). At 1.3 GPa, hornblende remnants exhibit rims of omphacitic clinopyroxene (**Fig. 5a**). In the matrix of these samples, aegyrine-rich, micrometric needles formed from the crystallization of the glass, together with quartz, rutile, a phengitic white mica, and minor pyrite and/or pyrrhotite (**Fig. 5a**). Plagioclase is not present in the assemblage at 1.3 GPa and the original muscovite flakes are rimmed by a newly formed white mica with a phengitic composition (Si = 3.41 pfu; **Table 5**). A sodic-calcic amphibole (katophorite) occurs in experiment #44 (**Table 5**). Pyrite or pyrrhotite are observed associated with ilmenite breakdown products. Biotite crystals are very rare at 1.3 GPa compared to the lower pressure experiments (only few small biotite crystals have been found in the matrix of experiment #43).

At lower pressures (0.7 – 1.15 GPa), titanite is the most stable Ti-rich phase (**Table 4**). However, again rutile needles may be seen to co-exist with titanite for the Ca-poorer compositions over this pressure interval, mostly rimming the ilmenite grains as shown in **Figures 5b and 5c** (see also **Table 4**). Ilmenite grains also exhibit replacement textures indicating dissolution from the rim towards the core, preferentially along apparent crystallographic planes (**Fig. 5c**). For Ca-richer compositions at lower pressure (e.g. GR3, 0.7 GPa), titanite directly rims ilmenite and rutile was not observed (**Table 4**; **Fig. 5d**). REE-enriched epidote, commonly found rimming allanite, is stable over the whole 0.7 to 1.3 GPa range. In two experiments (#41 and #42 at 1.3 GPa), a second generation of allanite rims the original allanite grain. This new allanite has a composition intermediate between the original allanite (c. 18 wt% REE; **Table 5**) and a REE-enriched epidote, with a lower REE concentration (approximately 12.5 wt% REE based on EDS analyses). The original hornblende grains, when preserved, reacted with the glass to form fine grained aggregates of biotite, titanite, and plagioclase for experiments up to 1.15 GPa.

Experiments at 450 °C

The three 450 °C experiments were run at pressures of 1.2, 1.4, and 1.6 GPa (**Fig. 6; Table 4**). At 1.6 GPa, no titanite was observed and original ilmenite grains exhibit spectacular replacement textures by rutile needles forming along apparent crystallographic planes (**Fig. 6a**) (see also Melcher, 1991). In the matrix (experiment #66; **Fig. 6b**), the original hornblende grains are rimmed by an aegyrine-rich clinopyroxene (**Table 5**). At lower pressure (1.4 GPa), titanite appears as a replacement product around ilmenite, together with sub-micrometric needles of rutile (**Fig. 6c**). In these experiments (#73-#76; 1.4 GPa), titanite volumetrically dominates over rutile within the Ca-richer compositions (#73 and #76) while rutile and titanite are observed in equal amounts (both in the matrix and around the ilmenite grains) in the Ca-poorer compositions (#75 and #74; **Table 4**).

At 1.2 GPa, titanite is dominant volumetrically over rutile (**Table 4**). Titanite is observed as 1 to 5 μm size crystals in the matrix in close proximity to the original hornblende grains, and also directly surrounding the ilmenite (**Fig. 6d**). Rutile has been observed in the Ca-poorest composition (1.2 GPa, #59) and always as sub-micron needles replacing ilmenite. Partially dissolved ilmenite grains show brighter rims with slightly higher Fe contents (**Fig. 6d**). The original allanite grains are rimmed by epidote (**Table 4**) and more rarely by titanite (in experiment #60 at 1.2 GPa). The matrix consists of a very fine-grained mixture of partly recrystallized granitoid glass, quartz, phengite (Si = 3.55-3.66 pfu; **Table 5**), sodic clinopyroxene, and pyrite. Hornblende seeds seem to be a reactive phase as they are commonly rimmed by a sodi-calcic clinopyroxene (omphacite or aegyrine; **Table 5**) over the entire pressure range (1.2 – 1.6 GPa; **Table 5; Fig. 6d**). Albite has been observed as 5 to 10 μm size crystals growing in the matrix

(experiment #57). A sodic, Fe-rich amphibole, in equilibrium with chlorite and titanite, has been observed in all the 450 °C experiments (over the entire pressure range) but no reliable composition could be obtained due to the small size of the grains and intergrowth with other phases. Some rare biotite crystals were also observed close to ilmenite at 1.4 GPa in experiment #74. Pyrite and pyrrhotite have been jointly observed at 450°C, both in the matrix and as replacement products around the original ilmenite grains.

DISCUSSION

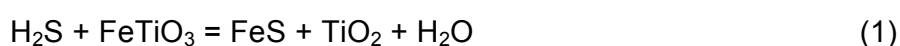
Interpretation of obtained textures

Despite the impossibility to reach fully equilibrated textures due to the sluggishness of reaction rates in the P-T range explored here (450-650°C), our work provides new insights into the P-T stability of titanite and rutile relative to ilmenite for granitoid and greywackes bulk compositions (as a function of whole rock X_{Ca}), metamorphosed during regional high-pressure metamorphism corresponding to subduction and collisional metamorphic gradients. Our results show that ilmenite is not stable in the range 450 to 650 °C and 0.7 to 1.6 GPa for the system studied here. Rather the ilmenite systematically exhibits textural evidence for dissolution and replacement by titanite at lower pressures and by rutile at higher pressures (**Fig. 7**) with both replacement textures accompanied by varying amounts of porosity. In our experiments, ilmenite replacement seemingly proceeds rapidly, in a matter of days or weeks, independent of the temperature chosen (e.g. **Fig. 6**) and thus appears more a function of the fluid reactivity rather than P-T.

These replacement textures, both from the experiments and from nature, preserve the outline of the original ilmenite grain during the replacement process (**Fig. 1d**; **Fig. 5a**)

and are a product of the coupling between the dissolution of ilmenite and the simultaneous reprecipitation of rutile and/or titanite (Putnis 2002, 2009; Putnis and Austrheim 2010). Owing to a negative volume difference during the conversion of ilmenite to titanite or rutile (-23% and -11% respectively), one of the outcomes of the replacement process is the production of a high porosity associated with micro-cracking, which in turn enhances the progression of the reaction front from the outer ilmenite rim towards the crystal core (e.g. **Fig. 6c**; see also the discussion in Putnis 2009).

In complex chemical environments, such as the one chosen for our experiments, as well as in natural systems, numerous reactions involving plagioclase, ilmenite, hornblende, or biotite may occur (e.g. Frost, 2001). In the particular chemical system covered by these experiments, three basic reactions, which involve the transformation of ilmenite to rutile and/or titanite in the presence of S, may be written. Indeed, the common occurrence of Fe sulphides (pyrite and pyrrhotite; e.g. **Fig. 5b**) in the vicinity of ilmenite pseudomorphs both in nature and in these experiments indicates that S appears to play an important role in helping to implement the replacement reaction (e.g. Tracy and Robinson 1988; Frost 1991), probably via the following three basic reactions:



Reaction (3) indicates that the formation of titanite from ilmenite requires the involvement of both S and Ca, most likely carried in the fluid phase. In addition to pyrite or pyrrhotite, the Fe released after ilmenite breakdown is also utilized in product biotite, epidote, and/or hornblende during the experiment (**Figs. 4c and 5c**). In the case of biotite, the dissolution-replacement of the ilmenite grains and breakdown of the muscovite flakes

releases the Fe, Si, Al, and K necessary for the growth of biotite within the ilmenite pseudomorphs. The formation of biotite in the vicinity of ilmenite/rutile aggregates has also been documented by Carswell and O'Brien (1993) for retrogressed granulites from the Bohemian massif. Under high-pressure conditions outside the biotite stability field, the Fe released during ilmenite breakdown may serve to enable the formation of Na-clinopyroxene (aegyrine or omphacite) close to the altered ilmenite (**Fig. 6b**).

At 650°C and 1.0 to 1.3 GPa, a granitic melt also formed, which is in equilibrium with rutile both within the partially replaced ilmenite grains and in the surrounding matrix (**Fig. 4d**; see also Xiong et al. 2005). The location and the shape of the melt-forming reaction curve identified here shares similarities with previous experimental work on melt formation in granitic systems under amphibolite-facies conditions (**Fig. 7**; e.g. Huang and Wyllie 1981; Schmidt 1993). Our experiments also indicate that the original allanite grains are systematically replaced by a lower-REE allanite or by REE-enriched epidote along their rims (see also Budzyn et al. 2011, 2017). The REE released during the dissolution of allanite outer rims are apparently partially incorporated by the newly forming titanite (see analysis #47-4 in Table 5; see also Spandler et al., 2003 and Harlov et al., 2006). Lastly, no systematic trend has been observed between the titanite Al content and the experimental confining pressure (see for example Harlov et al., 2006 or Trooper et al., 2002).

The importance of Ca activity in the system

These experiments demonstrate that the rutile-titanite stability field is influenced by the whole rock Ca concentration. Small rutile needles can form at low pressures (0.7-0.8 GPa), far within the titanite stability field, as a replacement product of ilmenite in Ca-poor

compositions (**Figs. 7 and 8; Table 4**). The absence of rutile in the Ca-richer experiments at these same pressures (c. 3 wt% CaO; experiments #37 and #40) and the presence of titanite confirm that the Ca activity in the system critically affects the formation of rutile.

As a consequence, we propose that rutile can be stable in Ca-poor systems as low as 0.7 GPa and possibly much lower depending on how low the actual whole rock Ca activity is. Conversely, for Ca-rich systems, the titanite stability field can be extended up to at least 1.3 GPa and possibly higher, depending on how high the Ca activity is (**Fig. 7**). It is also important to note the role of local Ca-activity gradients exerting a control over titanite and rutile stability. This local control is texturally visible in the vicinity of the allanite or hornblende seeds (14 and 12 wt% CaO, respectively) where thin overgrowths of titanite or epidote may be observed (e.g. **Fig. 4f**). Dissolution of these Ca-bearing phases locally increases the Ca availability in the system and promotes the localized growth of titanite at P-T conditions where rutile would normally be expected to prevail (e.g. experiments #45-#48). Note that the effect of this local Ca-enrichment disappears at higher pressures (typically above 1.5 GPa) where rutile is the only Ti-bearing phase stable in the experiment, independent of the immediate presence of allanite or hornblende seeds in the reaction volume. These results indicate that the presence of rutile, as an indicator of high-pressure metamorphic conditions, should only be used with great care and under specific mineralogical and geochemical conditions (see below). Similarly, the finding of titanite alone in a sample does not preclude a former high-pressure metamorphic event. The apparent absence of rutile may well indicate an episode of strong retrogression at lower pressure during exhumation or may simply be a product of the high Ca activity in the local rock system.

We also emphasize that natural rock systems may exhibit significant compositional heterogeneity on a localized scale, with Ca-enriched and Ca-depleted micro-domains, which may lead to the apparent co-stability of rutile and titanite in the same sample, as observed on a smaller scale in our experiments. As a consequence, mylonitic samples (**Fig. 1a**), that have undergone dynamic recrystallization, grain size reduction, and chemical homogenization would constitute appropriate sampling targets for studying the relative stabilities of rutile, titanite, and ilmenite as a function of P-T-X in order to avoid Ca content heterogeneity issues.

Applicability to natural systems and limitations

In high-pressure metamorphic rocks affected by exhumation-related recrystallization, aggregates of titanite with rutile cores are common (**Fig. 2**). This natural incomplete reaction texture may have formed during decompression via the reaction:



Our results indicate that for most granitoid compositions, the presence of rutile remnants may be used as a barometer to demonstrate that the rock underwent metamorphism at relatively high pressures and relatively low temperatures to burial depths in excess of ca. 40 km (**Fig. 7**). Note that the source of Ti in granitic systems may also come from the breakdown of other Ti-bearing minerals, such as hornblende or biotite, both of which can carry several wt% of TiO₂ (Ferry 1979; Gibbons and Horak 1984).

The pressure at which the rutile-in reaction occurs in our experiments is in relatively good agreement with the results from Liou et al (1998) for basaltic systems (as opposed to the granitic systems used in our experiments). These authors found that at 650°C, the rutile-titanite transition is expected to lie near 1.3 GPa, which is approximately

0.3 GPa higher than in our work (**Fig. 7**). This observation, made for a mafic system where the CaO concentration is three to four times higher than in our experiments, reveals that (i) the Ca activity does not alone control the formation of rutile or titanite, (ii) the buffering of a mineral assemblage in equilibrium with rutile or titanite has a major influence on phase relationships, and (iii) there are similarities between mafic and felsic systems with regard to the stability of rutile and/or titanite relative to ilmenite (e.g. Frost et al. 2001).

Numerous field and petrological studies have also shown that the stability of titanite and rutile, relative to ilmenite, is dramatically controlled by parameters other than bulk composition, pressure, and temperature variations. Systematically exploring the individual effects of each of these parameters is beyond the scope of this study. Among the most important factors, it is well-known that the presence of CO₂ in the fluid phase plays a role with regard to the breadth of the rutile and titanite stability field (Hunt and Kerrick 1977; Xirouchakis and Lindsley 1998). Titanite is known to preferentially form at low X(CO₂) values (Schuiling and Vick 1967). Carbon dioxide, which is not an abundant component within granitic environment fluids, has not been taken into account in our experiments. Yet, the CO₂ activity within metasedimentary systems (and more particularly within greywackes) is an additional factor and the results from the experiments presented here cannot be applied to any system containing carbonates. Titanite can also incorporate significant amounts of F as well as REE (e.g. Higgins and Ribbe, 1976; Table 5). Future work should investigate the influence of trace elements on the stability of titanite (see for instance Carswell et al., 1996; Tropper et al., 2002; Lucassen et al., 2010).

Similarly, oxygen fugacity variations during metamorphism may also play a critical role on the relative stabilities of titanite and rutile over the extent of the P-T-X_{Ca} field

considered in this study (e.g. Markl and Piazzolo 1999; Zhao et al. 1999; Harlov et al. 2006; René 2008). Natural samples from the Alps (Arolla gneiss) recrystallized under relatively low oxygen fugacity conditions as shown by the presence of a Fe-poor epidote (clinozoisite), by the presence of pyrite and by the presence of graphite in the underlying metasediments (Angiboust et al., 2014). The low oxygen fugacity of our experiments (graphite-CO-CO₂ buffer) is confirmed by the presence of pyrite, pyrrhotite or both (**Table 4**). However, no systematic trend was observed regarding the stability of pyrite and pyrrhotite relative to each other over the entire temperature and pressure range considered for the experiments (**Table 4**). The occasional apparent coexistence of these two minerals suggests that the oxygen fugacity conditions over the P-T range of our experiments remained close to the pyrrhotite-pyrite transition, i.e. $2\text{FeS} + 0.5\text{O}_2 = \text{FeS}_2 + \text{FeO}$. Further investigations should aim at better understanding the effect of changing oxygen fugacity on the stability of ilmenite breakdown products, namely rutile and titanite. For instance, the presence of reducing ultramafic rocks (abundant in subduction zone settings) or the influx of oxidizing fluids (e.g. Bali et al. 2011) may create local oxygen fugacity gradients, which could significantly affect the stability of rutile and titanite during metamorphism of the upper continental crust.

IMPLICATIONS

The presence of rutile cores in titanite is generally interpreted to indicate the existence of a retrograde event during exhumation that enabled the formation of titanite at the expense of rutile. The experiments in this study show that for normal granitic rocks, the presence of metamorphic rutile (along with other peak pressure minerals such as Si-rich phengite or Na-rich, blue amphibole in the matrix) can be considered as a good indicator of recrystallization at depths greater than ca. 40 km. Our work, aimed at reproducing

natural textures and providing an assessment of the P-T location of the rutile-titanite transition curve, paves the way for a systematic exploration of rock and fluid parameters (such as oxygen fugacity, sulphur fugacity, $X(\text{CO}_2)$, salinity, and pH of the fluid) that can influence the stability of rutile and titanite. Improving our understanding of rutile and titanite-forming processes in metamorphic rocks is important because these accessory minerals represent important thermometers and geo-chronometers (e.g. Essex & Gromet, 2000; Zack et al., 2011). The refinement of P-T-t paths will enable a better quantification of tectonic transport velocities and impact our understanding of large scale rheological processes in the Earth's lithosphere.

ACKNOWLEDGMENTS

The authors acknowledge W. Heinrich and M. Koch-Müller to provide access to the GFZ experimental laboratory. S. Herting-Agthe, B. Wunder and H-P. Nabein are thanked for technical assistance during experiments. C. Schmidt and J. Hermann are thanked for insightful advices and discussions. We acknowledge D. Rhede and O. Appelt for assistance with electron probe measurements. Emilie Janots and Mike Williams are warmly acknowledged for their constructive reviews. S.A. acknowledges the A. von Humboldt foundation for a post-doctoral grant that made this work possible. This is IPGP contribution #37XX.

REFERENCES CITED

- Angiboust, S., Kirsch, J., Oncken, O., Glodny, J., Monié, P., and Rybacki, E. (2015) Probing the transition between seismically coupled and decoupled segments along an ancient subduction interface. *Geochemistry Geophysics Geosystems*, 16(6), 1905-1922.
- Angiboust, S., Glodny, J., Oncken, O., and Chopin, C. (2014) In search of transient subduction interfaces in the Dent Blanche–Sesia Tectonic System (W. Alps). *Lithos*, 205, 298-321.
- Auzanneau, E., Vielzeuf, D., and Schmidt, M.W. (2006) Experimental evidence of decompression melting during exhumation of subducted continental crust. *Contributions to Mineralogy and Petrology*, 152(2), 125-148.
- Bali, E., Audétat, A., and Keppler, H. (2011) The mobility of U and Th in subduction zone fluids: an indicator of oxygen fugacity and fluid salinity. *Contributions to Mineralogy and Petrology*, 161(4), 597-613.
- Blatt, H. and Tracy, R. J. (1996) *Petrology. Igneous, Sedimentary, and Metamorphic*, 2nd ed. 529 pp. New York, Basingstoke: W. H. Freeman and Co.
- Bucher, S. and Bousquet, R. (2007) Metamorphic evolution of the Briançonnais units along the ECORS-CROP profile (Western Alps): new data on metasedimentary rocks. *Swiss Journal of Geosciences*, 100(2), 227-242.
- Budzyń, B., Harlov, D.E., Williams, M.L., and Jercinovic, M.J. (2011) Experimental determination of stability relations between monazite, fluorapatite, allanite, and REE-epidote as a function of pressure, temperature, and fluid composition. *American Mineralogist*, 96(10), 1547-1567.
- Budzyń, B., Harlov, D.E., Kozub-Budzyń, G.A., and Majka, J. (2017) Experimental constraints on the relative stabilities of the two systems monazite-(Ce) – allanite-(Ce) – fluorapatite and xenotime-(Y) – (Y,HREE)-rich epidote – (Y,HREE)-rich fluorapatite, in high Ca and Na-Ca environments under P-T conditions of 200–1000 MPa and 450–750 °C. *Mineralogy and Petrology*, 111(2), 183-217.
- Burri, M. (1983) Le front du Grand St-Bernard du val d'Hérens au val d'Aoste. *Eclogae Geologicae Helvetiae*, 76(3), 469-490.
- Carswell, D.A., and O'Brien, P.J. (1993) Thermobarometry and geotectonic significance of high-pressure granulites: examples from the Moldanubian Zone of the Bohemian Massif in Lower Austria. *Journal of Petrology*, 34(3), 427-459.
- Carswell, D.A., Wilson, R.N. and Zhai, M. (1996) Ultra-high pressure aluminous titanites in carbonate-bearing eclogites at Shuanghe in Dabieshan, central China. *Mineralogical Magazine*, 60(3), 461-471.
- Compagnoni, R. (1977) The Sesia-Lanzo Zone: high pressure-low temperature metamorphism in the Austroalpine continental margin. *Rendiconti Società Italiana Mineralogia e Petrologia*, 33, 335-374.

- Compagnoni, R., Hirajima, T., and Chopin, C. (1995) Ultra-high-pressure metamorphic rocks in the Western Alps. *Ultrahigh pressure metamorphism*, 206-243.
- Dal Piaz, G., Cortiana, G., Del Moro, A., Martin, S., Pennacchioni, G., and Tartarotti, P. (2001) Tertiary age and paleostructural inferences of the eclogitic imprint in the Austroalpine outliers and Zermatt–Saas ophiolite, western Alps. *International Journal of Earth Sciences*, 90(3), 668-684.
- Essex, R.M., and Gromet, L.P. (2000). U-Pb dating of prograde and retrograde titanite growth during the Scandian orogeny. *Geology*, 28(5), 419-422.
- Evans, B W. (1990) Phase relations of epidote-blueschists. *Lithos*, 25(1), 3-23.
- Evans, B.W., and Patrick, B.E. (1987) Phengite-3T in high-pressure metamorphosed granitic orthogneisses, Seward Peninsula, Alaska. *Canadian Mineralogist*, 25, 141-158.
- Ferry, J.M. (1979) Reaction mechanisms, physical conditions, and mass transfer during hydrothermal alteration of mica and feldspar in granitic rocks from south-central Maine, USA. *Contributions to Mineralogy and Petrology*, 68(2), 125-139.
- Frey, M., and Mählmann, R. (1999) Alpine metamorphism of the Central Alps. *Schweizerische Mineralogische Petrography*, 79(1), 135-154.
- Frost, B.R., Chamberlain, K.R., and Schumacher, J.C. (2001) Sphene (titanite): phase relations and role as a geochronometer. *Chemical Geology*, 172(1), 131-148.
- Frost, B.R. (1991) Stability of oxide minerals in metamorphic rocks. *Reviews in Mineralogy and Geochemistry*, 25(1), 469-488.
- Gabudianu Radulescu, I., Rubatto, D., Gregory, C., and Compagnoni, R. (2009) The age of HP metamorphism in the Gran Paradiso Massif, Western Alps: a petrological and geochronological study of “silvery micaschists”. *Lithos*, 110(1), 95-108.
- Gaggero, L., Buzzi, L., Haydoutov, I., and Cortesogno, L. (2009) Eclogite relics in the Variscan orogenic belt of Bulgaria (SE Europe) *International Journal of Earth Sciences*, 98(8), 1853-1877.
- Ganne, J., Bussy, F., and Vidal, O. (2003) Multi-stage garnet in the internal Briançonnais basement (Ambin Massif, Savoy): new petrological constraints on the blueschist-facies metamorphism in the Western Alps and tectonic implications. *Journal of Petrology*, 44(7), 1281-1308.
- Gasser, D., Jeřábek, P., Faber, C., Stünitz, H., Menegon, L., Corfu, F., et al (2015) Behaviour of geochronometers and timing of metamorphic reactions during deformation at lower crustal conditions: phase equilibrium modelling and U–Pb dating of zircon, monazite, rutile and titanite from the Kalak Nappe Complex, northern Norway. *Journal of Metamorphic Geology*, 33(5), 513-534.

- Gibbons, W.E.S., and Horak, J. (1984) Alpine metamorphism of Hercynian hornblende granodiorite beneath the blueschist facies schistes lustrés nappe of NE Corsica. *Journal of Metamorphic Geology*, 2(2), 95-113.
- Harlov, D., Tropper, P., Seifert, W., Nijland, T., and Förster, H.J. (2006) Formation of Al-rich titanite ($\text{CaTiSiO}_4\text{O}-\text{CaAlSiO}_4\text{OH}$) reaction rims on ilmenite in metamorphic rocks as a function of $f\text{H}_2\text{O}$ and $f\text{O}_2$. *Lithos*, 88(1), 72-84.
- Higgins, J.B. and Ribbe, P.H., 1976. The crystal chemistry and space groups of natural and synthetic titanites. *American Mineralogist*, 61, 878–888.
- Huang, W.L., and Wyllie, P.J. (1981) Phase relationships of S-type granite with H_2O to 35 kbar: Muscovite granite from Harney Peak, South Dakota. *Journal of Geophysical Research: Solid Earth*, 86(B11), 10515-10529.
- Hunt, J.A., and Kerrick, D.M. (1977) The stability of sphene; experimental redetermination and geologic implications. *Geochimica Cosmochimica Acta*, 41(2), 279-288.
- Johannes, W., Bell, P. M., Mao, H. K., Boettcher, A. L., Chipman, D. W., Hays, J. F., et al. (1971) An interlaboratory comparison of piston-cylinder pressure calibration using the albite-breakdown reaction *Contributions to Mineralogy and Petrology*, 32(1), 24-38.
- Johannes, W. (1973) A simplified piston-cylinder apparatus of high precision. *Neues Jahrbuch Mineralogisch Monatlich*, 7(8), 331-351.
- Konrad-Schmolke, M., O'Brien, P. J., and Zack, T. (2011) Fluid migration above a subducted slab—constraints on amount, pathways and major element mobility from partially overprinted eclogite-facies rocks (Sesia Zone, Western Alps). *Journal of Petrology*, 52(3), 457-486.
- Kylander-Clark A.R.C., Hacker B.R., and Mattinson J.M. (2008) Slow exhumation of UHP terranes: titanite and rutile ages of the Western Gneiss Region, Norway. *Earth and Planetary Science Letters*, 272(3), 531-540.
- Lardeaux, J M., and Spalla, M.I. (1991) From granulites to eclogites in the Sesia zone (Italian Western Alps): a record of the opening and closure of the Piedmont ocean. *Journal of Metamorphic Geology*, 9(1), 35-59.
- Leake, B. E. (1978) Nomenclature of amphiboles. *Canadian Mineralogist*, 16(4), 501-520.
- Le Maitre, R. W. (1976) The chemical variability of some common igneous rocks. *Journal of Petrology*, 17(4), 589-598.
- Liou, J.G., Zhang, R. Y., Ernst, W. G., Liu, J., and McLimans, R. (1998) Mineral parageneses in the Piampaludo eclogitic body, Gruppo di Voltri, western Ligurian Alps. *Schweizerisch Mineralogische Petrographi Mittelungen*, 78(2), 317-335.

- Lombardo, B., Compagnoni, R., Fiora, L., and Facchinelli, A. (1977) Composition of some sodic pyroxenes from the eclogitic micaschists of lower Val d'Aosta (Sesia Lanzo zone, Western Alps). *Rendiconti Societa Italiana de Mineralogia e Petrografia*, 33, 375-387.
- Lucassen, F., Franz, G., Dulski, P., Romer, R. L., and Rhede, D. (2011) Element and Sr isotope signatures of titanite as indicator of variable fluid composition in hydrated eclogite. *Lithos*, 121(1), 12-24.
- Luvizotto, G. L., Zack, T., Triebold, S., and Von Eynatten, H. (2009) Rutile occurrence and trace element behavior in medium-grade metasedimentary rocks: example from the Erzgebirge, Germany. *Mineralogy and Petrology*, 97(3-4), 233-249.
- Markl, G., and Piazzolo, S. (1999) Stability of high-Al titanite from low-pressure calcsilicates in light of fluid and host-rock composition. *American Mineralogist*, 84(1-2), 37-47.
- Marquer, D. (1990) Structures et déformation alpine dans les granites hercyniens du massif du Gothard (Alpes centrales suisses). *Eclogae Geologie Helvetiana*, 83(1), 77-97.
- Massonne, H. J. (2015) Derivation of P–T paths from high-pressure metagranites—Examples from the Gran Paradiso Massif, western Alps. *Lithos*, 226, 265-279.
- Meinhold, G. (2010) Rutile and its applications in earth sciences. *Earth Science Reviews*, 102(1), 1-28.
- Melcher, F. (1991) Fe-Ti-Oxide Assemblages in the Basal Parts of the Central Alpine Brenner Mesozoic, Tyrol/Austria. *Mineralogy and Petrology*, 44, 197-212.
- Morimoto, N. (1988) Nomenclature of pyroxenes. *Mineralogy and Petrology*, 39(1), 55-76.
- Nussbaum, C., Marquer, D., and Biino, G. G. (1998) Two subduction events in a polycyclic basement: Alpine and pre-Alpine high-pressure metamorphism in the Suretta nappe, Swiss Eastern Alps. *Journal of Metamorphic Geology*, 16(5), 591-605.
- Pearce M. A., and Wheeler J. (2014) Microstructural and Metamorphic Constraints on the Thermal Evolution of the Southern Region of the Lewisian Gneiss Complex, NW Scotland. *Journal of Petrology*, 55(10), 2043-2066.
- Pennacchioni, G., and Guermani, A. (1993) The mylonites of the Austroalpine Dent Blanche nappe along the northwestern side of the Valpelline Valley (Italian Western Alps) *Memorie Scienze Geologica*, 45, 37-55.
- Proyer, A. (2003) The preservation of high-pressure rocks during exhumation: metagranites and metapelites. *Lithos*, 70(3), 183-194.
- Putnis, A. (2002) Mineral replacement reactions: from macroscopic observations to microscopic mechanisms. *Mineralogical Magazine*, 66(5), 689-708.

- Putnis, A. (2009) Mineral replacement reactions. *Reviews in mineralogy and geochemistry*, 70(1), 87-124.
- Putnis, A., and Austrheim, H. (2010) Fluid-induced processes: metasomatism and metamorphism. *Geofluids*, 10, 254–269.
- Rene, M. (2008) Titanite-ilmenite-magnetite phase relations in amphibolites of the Chynov area (Bohemian massif, Czech Republic). *Acta Geodynamica Geomat*, 5(3), 239-247.
- Roda, M., and Zucali, M. (2011) Tectono-metamorphic map of the Mont Morion Permian metaintrusives (Mont Morion—Mont Collon—Matterhorn Complex, Dent Blanche Unit), Valpelline—Western Italian Alps. *Journal of Maps*, 7(1), 519-535.
- Rolland, Y., Cox, S., Boullier, A. M., Pennacchioni, G., and Mancktelow, N. (2003) Rare earth and trace element mobility in mid-crustal shear zones: insights from the Mont Blanc Massif (Western Alps). *Earth and Planetary Science Letters*, 214(1), 203-219.
- Rubbo, M., Borghi, A. and Compagnoni, R. (1999) Thermodynamic analysis of garnet growth zoning in eclogite facies granodiorite from M. Mucrone, Sesia Zone, Western Italian Alps. *Contributions to Mineralogy and Petrology*, 137(4), 289-303.
- Rudnick, R. L., and Fountain, D. M. (1995) Nature and composition of the continental crust: a lower crustal perspective. *Review in geophysics*, 33(3), 267-309.
- Sanchez, G., Rolland, Y., Schneider, J., Corsini, M., Oliot, E., Goncalves, P., and Marquer, D. (2011) Dating low-temperature deformation by $^{40}\text{Ar}/^{39}\text{Ar}$ on white mica, insights from the Argentera-Mercantour Massif (SW Alps). *Lithos*, 125(1), 521-536.
- Schmidt M. W. (1993) Phase relations and compositions in tonalite as a function of pressure: an experimental study at 650 C. *American Journal of Science*, 293, 1001-1011.
- Schulling, R. D, and Vink, B. W. (1967) Stability relations of some titanium-minerals (sphene, perovskite, rutile, anatase). *Geochimica cosmochimica acta*, 31(12), 2399-2411.
- Smye, A. J., and Stockli, D. F. (2014) Rutile U–Pb age depth profiling: A continuous record of lithospheric thermal evolution. *Earth and Planetary Science Letters*, 408, 171-182.
- Spandler, C. Hermann, J., Arculus, R. and Mavrogenes, J. (2003). Redistribution of trace elements during prograde metamorphism from lawsonite blueschist to eclogite facies; implications for deep subduction-zone processes. *Contributions to Mineralogy and Petrology*, 146(2), 205-222.

- Tracy, R. J., and Robinson, P. (1988) Silicate-sulfide-oxide-fluid reactions in granulite-grade pelitic rocks, central Massachusetts. *American Journal of Science*, 288, 45-74.
- Tricart, P. (1984) From passive margin to continental collision; a tectonic scenario for the Western Alps. *American Journal of Science*, 284(2), 97-120.
- Tropper, P., Essene, E. J., Sharp, Z. D., and Hunziker, J. C. (1999) Application of K-feldspar-jadeite-quartz barometry to eclogite facies metagranites and metapelites in the Sesia Lanzo Zone (Western Alps, Italy). *Journal of Metamorphic Geology*, 17, 195-210.
- Tropper, P., Manning, C. E. and Essene, E. J. (2002) The substitution of Al and F in titanite at high pressure and temperature: experimental constraints on phase relations and solid solution properties. *Journal of Petrology*, 43(10), 1787-1814.
- Tropper, P., and Manning, C. E. (2008). The current status of titanite–rutile thermobarometry in ultrahigh-pressure metamorphic rocks: the influence of titanite activity models on phase equilibrium calculations. *Chemical Geology*, 254(3), 123-132.
- Whitney, D. L., and Evans, B. W. (2010) Abbreviations for names of rock-forming minerals. *American mineralogist*, 95(1), 185-190.
- Xiong, X. L., Adam, J., and Green, T. H. (2005) Rutile stability and rutile/melt HFSE partitioning during partial melting of hydrous basalt: implications for TTG genesis. *Chemical Geology*, 218(3), 339-359.
- Xirouchakis, D., and Lindsley, D. H. (1998) Equilibria among titanite, hedenbergite, fayalite, quartz, ilmenite, and magnetite: experiments and internally consistent thermodynamic data for titanite. *American Mineralogist*, 83(7-8), 712-725.
- Zack, T., Moraes, R., and Kronz, A. (2004) Temperature dependence of Zr in rutile: empirical calibration of a rutile thermometer. *Contributions to Mineralogy and Petrology*, 148(4), 471-488.
- Zack, T., Stockli, D. F., Luvizotto, G. L., Barth, M. G., Belousova, E., Wolfe, M. R., and Hinton, R. W. (2011). In situ U–Pb rutile dating by LA-ICP-MS: 208Pb correction and prospects for geological applications. *Contributions to Mineralogy and Petrology*, 162(3), 515-530.
- Zhao, D., Essene, E. J., and Zhang, Y. (1999) An oxygen barometer for rutile–ilmenite assemblages: oxidation state of metasomatic agents in the mantle. *Earth and Planetary Science Letters*, 166(3), 127-137.

Figure captions

Figure 1. (a). Polished slab showing a representative Arolla gneiss sample with moderate mylonitic deformation (dashed line). Chl: chlorite; Ep: epidote; Ab: albite; Ph: phengite; Qz: quartz. **(b-d).** BSE images showing microstructural relationships between ilmenite, rutile, and titanite from high pressure metagranitoids from the Arolla gneiss (Dent Blanche nappe, W. Alps: locality: Arolla, Switzerland). **(b).** Back-scattered (BSE-SEM) image showing relicts of ilmenite, rimmed by rutile, and preserved in the middle of a large titanite porphyroclast. **(c).** BSE image showing pseudomorphs after ilmenite that are occasionally visible as skeleton-shaped, porous domains replaced and rimmed by rutile. Titanite always surrounds rutile. **(d).** Pseudomorph after ilmenite showing dissolution and rutile replacing ilmenite. Note the large amount of porosity (black) formed during the replacement process. A micro-fracture lined with small rutile crystals is visible. Titanite rims the whole assemblage, per usual within the Arolla gneiss

Figure 2. (a). QAP Streckeisen diagram showing the normative composition (calculated using the CIPW norm) for the starting granitoid glasses (GR1 to GR4). Average granite composition is from Blatt and Tracy (1996). Bulk continental crust composition is from Rudnick and Fountain (1995). **(b).** Ternary plot showing the distribution of experimental material and average felsic compositions from the literature (greywacke from Auzanneau et al. 2006) in the SiO₂-FeO-CaO system. The grey shaded area corresponds to bulk rock analyses from the base of the Arolla unit (Dent Blanche massif) from which the starting material is derived (data from Angiboust et al. 2015)

Figure 3. Sketch of the NaCl assembly used in the experiments with the piston-cylinder apparatus

Figure 4. High contrast BSE images of ilmenite-rutile-titanite textures obtained experimentally at 650°C. Italicized labels refer to crystals introduced as mineral nuclei in the starting granitoid glass before the start of the experiment (e.g. *Ilm*, *Aln* or *Hbl*). **(a)**. Replacement of ilmenite (*Ilm*) by rutile (*Rt*) along a fracture. **(b)**. Overgrowth of hornblende (*Hbl*) by omphacite (*Omp*). **(c)**. Pseudomorph after ilmenite almost completely transformed to a complex aggregate of rutile and biotite (*Bt*) needles. **(d)**. Pseudomorph after ilmenite surrounded by a thin rutile rim and filled with bleb-like crystalline remnants of the original ilmenite and a granitoid melt. The location of an EMP analysis point of this melt is visible next to the melt label. **(e)**. Crystallization of small, euhedral titanite (*Ttn*) crystals in close association with biotite within the recrystallized granitoid matrix. **(f)**. Allanite (*Aln*) crystal showing partial dissolution accompanied by depletion of REE and formation of porosity. Epidote (*Ep*) and titanite are seen growing along the rim of the allanite grain intergrown with biotite

Figure 5. High contrast BSE images of ilmenite-rutile-titanite textures obtained at 550°C. Italicized labels refer to mineral grains introduced as nuclei in the original granitoid glass before the start of the experiment (e.g. ilmenite (*Ilm*), allanite (*Aln*), or hornblende (*Hbl*)). **(a)**. Picture showing the complete dissolution and replacement of ilmenite by a network of rutile (*Rt*) needles accompanied by a great deal of porosity. In the surrounding mineral matrix omphacite (*Omp*), phengite (*Ph*), and pyrrhotite (*Po*) are visible. **(b)**. Replacement of ilmenite by rutile, and replacement of muscovite (*Ms*) by biotite (*Bt*) in the mineral

matrix. Pyrite (Py) is visible in the vicinity of the ilmenite pseudomorphs. **(c)**. Ilmenite partially replaced and rimmed by rutile. The reaction front between the altered and unaltered ilmenite is outlined by small titanite (Ttn) crystals. Biotite flakes also grow in the vicinity of the ilmenite. **(d)**. Partial dissolution of ilmenite replaced by titanite and biotite at 0.7 GPa

Figure 6. High contrast BSE images of ilmenite-rutile-titanite textures obtained at 450°C. Italicized labels refer to ilmenite (Ilm), allanite (Aln), and hornblende (Hbl) mineral grains introduced as nuclei in the starting granitoid glass before the start of the experiment. **(a)**. Picture showing complete replacement of ilmenite by a dense network of rutile (Rt) needles accompanied by a large amount of porosity. **(b)**. Representative view of the mineral matrix showing starting hornblende grains rimmed by an omphacitic clinopyroxene (Omp), and rutile growing at the expense of ilmenite. **(c)**. Partial dissolution of ilmenite and replacement by a fine-grained mixture of rutile needles and titanite (Ttn) crystals (see inset). Ilmenite breakdown led to the formation of voids in the reaction zone. **(d)**. Picture showing ilmenite dissolution with accompanying porosity and growth of a titanite rim, and overgrowth of omphacitic clinopyroxene around hornblende starting grains

Figure 7. Pressure-temperature diagram showing results obtained for both the Ca-rich (c. 3% CaO) and Ca-poor (c. 1% CaO) experiments (Table 4). At higher pressures, titanite was not observed (either in the matrix nor as an ilmenite replacement product; red boxes). At lower pressure, rutile is absent from the Ca-rich experiments (green boxes) but may be observed down to 0.7 GPa for Ca-poor compositions (e.g. #37–#40).

At the medium pressures for each temperature, titanite and rutile may co-exist together, though this is ultimately also a function of the Ca activity in the experiment. We also plot the curve corresponding to newly formed melt in experiments #45–#48 and #61–#64 and the Na-clinopyroxene forming reaction curve. Metamorphic facies grid in the background of the figure is modified after Evans (1990). GS: greenschist-facies; BS: blueschist-facies; EBS: epidote-blueschist facies; EA: epidote amphibolite; A: amphibolite; ECL: eclogite

Figure 8. Sketch showing micro-textural relationships between the various mineral species at 550 °C and 1 GPa (for both Ca-rich and Ca-poor compositions) and at 1.3 GPa. At 1.0 GPa, the availability of Ca in the system (as well as local Ca-producing processes such as allanite dissolution) play a critical role regarding the formation of either titanite or rutile. In Ca-poor compositions, titanite and rutile are often observed co-existing within and around ilmenite pseudomorphs. For Ca-rich whole rock compositions at 1.0 GPa, rutile is not observed in the experimental product. At 1.3 GPa for Ca-rich whole rock compositions, rutile is ubiquitous and titanite is not observed in the experimental product

Table captions

Table 1. Summary of some natural observations from exhumed metagranitoids from the W. Alps reporting the nature of the main Ti-bearing phase as a function of calculated pressure and temperature. References: [1] Marquer 1990 [2] Frey and Mählmann 1999 and references therein [3] Rolland et al. 2003 [4] Sanchez et al. 2011 [5] Nussbaum et al. 1998 [6] Burri 1983 [7] Bucher and Bousquet 2007 [8] Lardeaux and Spalla 1991 [9]

Angiboust et al. 2014 [10] Roda and Zucali 2011 [11] Ganne et al. 2003 [12]
 Compagnoni 1977 [13] Konrad-Schmolke et al. 2011 [14] Lombardo et al. 1977 [15]
 Rubbo et al. 1999 ; [16] Trooper et al. 1999 [17] Gabudianu Radulescu et al. 2009 [18]
 Compagnoni et al. 1995

TABLE 1. Natural occurrences of titanite and rutile in the W. Alps

<i>Granitoid natural occurrence</i>	Peak metamorphic conditions			<i>Ref.</i>
	<i>main Ti-bearing phase</i>	<i>P (GPa)</i>	<i>T (°C)</i>	
<i>Gothard massif</i>	Titanite	0.4	400-450	[1] [2]
<i>Mont Blanc shear zone</i>	Titanite	0.5	400	[3]
<i>Mercantour granitic mylonite</i>	Titanite	0.5-0.7	350-400	[4]
<i>Suretta nappe</i>	Titanite	1	400-450	[5]
<i>Ruitor zone</i>	Titanite	1.2	450	[6] [7]
<i>Gneiss minuti</i>	Rutile	1-1.5	500-550	[8]
<i>Arolla gneiss</i>	Rutile	1.2-1.4	400-500	[9] [10]
<i>Ambin dome</i>	Rutile/Titanite	1.5	500	[11] [12]
<i>Sesia Eclogitic Micaschist Complex</i>	Rutile	1.5-2	550	[13]
<i>Sesia Eclogitic Complex orthogneiss</i>	Titanite	1.5-2	550	[14]
<i>Monte Mucrene metagranitoid (Sesia)</i>	Rutile	1.6-2	550	[15]
<i>Silvery micaschists (Gran Paradiso)</i>	Rutile	1.9-2.7	515-600	[16]
<i>Brossasco-Issasca unit (Dora Maira)</i>	Rutile	3.0-3.6	720-780	[17]

Table 2. Major element composition (XRF) of a suite of metagranitoids from the Arolla unit (Dent Blanche Massif, W. Alps; Angiboust et al. 2015)

TABLE 2. Bulk rock composition of natural samples and experimental material

<i>rock type</i>	<i>meta-granitoid</i>	<i>meta-granitoid</i>	<i>meta-granitoid</i>	<i>Arolla mylonite</i>	<i>Arolla mylonite n</i>				
<i>sample ref.</i>	#54C	#67C	#67A	#34S	#05E	#34C	#35E	#12I	#35K
<i>glass ref.</i>	GR1	GR2	GR3	GR4	-	-	-	-	-
SiO ₂	77.50	71.70	70.30	66.21	77.43	60.40	63.00	68.90	60.10
TiO ₂	0.08	0.32	0.25	0.42	0.09	0.59	0.67	0.53	0.62

Al ₂ O ₃	11.80	13.40	14.60	15.89	12.24	18.00	16.40	13.50	16.90
Fe ₂ O ₃	0.55	2.05	1.87	2.62	1.04	3.68	3.43	2.11	2.91
FeO	0.41	1.03	0.58	0.89	n.a.	1.15	1.76	2.74	2.57
MnO	0.03	0.06	0.05	0.06	0.03	0.08	0.09	0.09	0.12
MgO	0.32	0.79	1.03	1.25	0.3	1.73	2.27	2.62	2.74
CaO	0.47	2.38	1.12	3.19	0.69	4.59	2.66	0.91	3.36
Na ₂ O	3.25	2.93	2.85	4.22	3.13	4.73	5.01	3.69	5.44
K ₂ O	4.38	3.41	5.26	2.75	4.24	1.91	1.61	1.68	1.91
P ₂ O ₅	0.02	0.08	0.07	0.12	0.02	0.18	0.25	0.15	0.19
H ₂ O	0.85	1.36	1.68	1.31	0.45	2.25	2.36	2.58	2.31
CO ₂	0.05	0.21	0.11	0.05	0.14	0.06	0.07	0.14	0.16
<i>Total</i>	99.75	99.81	99.85	98.99	99.80	99.53	99.74	99.85	99.62

Table 3. EMP analyses of starting material (glass) and starting minerals (Ilm, Hbl, Ms and Aln). Fe₂O₃ calculated by stoichiometry

TABLE 3. Composition of starting glass material and mineral seeds

	<i>glass</i> GR1	<i>glass</i> GR2	<i>glass</i> GR3	<i>glass</i> GR4	<i>Ilm</i>	<i>Hbl</i>	<i>Ms</i>	<i>Aln</i>
					starting material			
SiO₂	66.89	68.04	65.44	64.92	0.05	39.36	46.29	31.66
TiO₂	0.03	0.32	0.38	0.48	52.15	3.61	0.43	0.24
Al₂O₃	16.68	15.02	15.35	15.72	1.01	13.59	34.71	19.19
Fe₂O₃*	n.a.	n.a.	n.a.	n.a.	4.03	0.01	0.00	14.03
FeO	0.84	2.62	3.49	3.70	36.20	10.49	3.79	0.00
MnO	0.06	0.05	0.09	0.08	0.12	0.12	0.04	0.25
MgO	0.41	1.30	1.14	1.42	5.97	12.97	0.51	0.98
CaO	0.89	1.35	3.29	3.47	0.00	12.01	0.00	13.97
Na₂O	5.15	3.27	3.57	4.70	0.01	2.01	1.04	0.03
K₂O	6.66	5.77	4.01	3.04	0.00	2.33	8.74	ΣREE 17.90
Total	97.60	97.75	96.76	97.53	99.54	96.50	95.56	98.25

Table 4. Summary of paragenesis observed within experiments and mineral replacement products after ilmenite

TABLE 4. Experimental conditions and starting materials (mg)

Experiment	P (GPa)	T (°C)	Time (d)	GR1 0.5% CaO	GR2 1.1% CaO	GR3 2.4% CaO	GR4 3.2% CaO
#55	0.8	650	16	17.23			
#54	0.8	650	16		15.42		
#53	0.8	650	16			13.52	
#56	0.8	650	16				13.74
#47	1.0	650	21	12.70			
#46	1.0	650	21		14.21		
#45	1.0	650	21			14.01	
#48	1.0	650	21				13.89
#63	1.3	650	20	12.88			
#62	1.3	650	20		14.30		
#61	1.3	650	20			15.85	
#64	1.3	650	20				14.97
#31	1.6	650	21		11.60		
#30	1.6	650	21			6.90	
#39	0.7	550	21	12.84			
#38	0.7	550	21		10.97		
#37	0.7	550	21			11.68	
#40	0.7	550	21				14.73
#35	1.0	550	24	17.20			
#34	1.0	550	24		12.60		
#33	1.0	550	24			12.90	
#36	1.0	550	24				14.60
#51	1.15	550	21	14.57			
#50	1.15	550	21		15.02		
#49	1.15	550	21			13.13	
#52	1.15	550	21				12.51
#43	1.3	550	21	11.97			
#42	1.3	550	21		9.86		

#41	1.3	550	21		12.45	
#44	1.3	550	21			13.45
#59	1.2	450	42	13.45		
#58	1.2	450	42		12.53	
#57	1.2	450	42			14.03
#60	1.2	450	42			15.00
#75	1.4	450	11	11.63		
#74	1.4	450	11		12.56	
#73	1.4	450	11			14.20
#76	1.4	450	11			12.97
#67	1.6	450	56	15.76		
#66	1.6	450	56		15.05	
#65	1.6	450	56			12.64
#68	1.6	450	56			15.85

Table 5. Summary of EMP analyses of mineral species formed during the experiments. Amphibole and clinopyroxene composition calculated following Leake et al. (1978) and Morimoto (1988), respectively

TABLE 5. Composition of experimental products

<i>experiment</i>	#45	#45	#47	#47	#62	#61	#64	#64	#31	#31
<i>reference</i>	6	10	21	4	1	3	10	12	69	2
<i>mineral</i>	<i>Ttn</i>	<i>melt</i>	<i>melt</i>	<i>Ttn</i>	<i>Ttn</i>	<i>Ep</i>	<i>Bt</i>	<i>Hbl</i>	<i>Rt</i>	<i>Aeg</i>
T=650°C										
<i>P (GPa)</i>	1.0	1.0	1.0	1.0	1.3	1.3	1.3	1.3	1.6	1.6
SiO₂	30.31	67.46	69.93	27.58	30.57	38.97	38.42	42.92	0.01	52.62
TiO₂	36.97	0.47	0.52	35.01	37.86	0.86	2.65	1.50	95.94	0.77
Al₂O₃	0.84	13.01	13.31	1.39	1.69	24.63	15.70	13.21	0.15	4.40
Fe₂O₃	-	-	-	-	-	10.12	-	-	-	-
FeO	1.38	0.88	0.70	1.45	1.51	0.00	17.57	17.09	3.41	20.96
MnO	0.01	0.02	0.01	0.06	0.00	0.23	0.11	0.26	0.00	0.26
MgO	0.00	0.05	0.03	0.23	0.00	0.02	10.63	7.87	0.00	2.95
CaO	28.15	0.53	0.42	25.78	27.94	23.18	0.00	8.90	0.03	8.09
Na₂O	0.09	4.30	1.69	0.16	0.00	0.00	0.31	4.01	0.18	9.39

K₂O	0.10	2.59	3.11	n.a.	0.00	0.00	8.90	0.93	0.02	0.00
ΣREE	n.a.	n.a.	n.a.	1.12	n.a.	n.a.	n.a.	n.a.	n.a.	n.a.
Total	97.85	89.31	89.73	92.78	99.57	98.01	94.30	96.69	99.74	99.44

X_{ps}=21 X_{Mg}=0.52 Si=6.49
 Na=1.18
 Qua₃₁
 Jd₁₉
 Aeg₅₀

T=550°C	<i>experiment</i>	#39	#34	#34	#51	#44	#43	#44	#43	#43
	<i>reference</i>	54	1	2	82	32	50	52	42	47
	<i>mineral</i>	Rt	Ttn	Bt	Bt	Ep	Phg	Amp	Aeg	Omp
	P (GPa)	0.7	1.0	1.0	1.15	1.3	1.3	1.3	1.3	1.3
	SiO₂	0.22	30.04	39.25	38.95	37.72	49.30	46.87	54.55	54.78
	TiO₂	94.94	35.12	2.50	3.69	1.31	1.72	0.60	2.39	1.50
	Al₂O₃	0.06	1.90	16.97	12.83	23.46	20.59	9.33	7.81	7.40
	Fe₂O₃	-	-	-	-	11.79	-	-	-	-
	FeO	2.72	1.45	19.36	21.25	0.00	9.81	18.87	15.47	8.52
	MnO	0.01	0.05	0.13	0.16	0.21	0.05	0.24	0.11	0.31
	MgO	0.01	0.00	7.35	7.95	0.14	4.40	7.90	2.40	7.18
	CaO	0.06	27.30	0.04	0.00	22.56	0.00	5.45	4.43	10.72
	Na₂O	0.10	0.12	0.40	0.25	0.09	0.25	5.39	11.68	7.60
	K₂O	0.05	0.24	9.12	9.35	0.03	9.78	0.44	0.02	0.26
ΣREE	n.a.	n.a.	n.a.	n.a.	n.a.	n.a.	n.a.	n.a.	n.a.	
Total	97.98	96.22	95.12	94.43	97.31	95.90	95.10	98.86	98.26	

X_{ps}=24 Si=3.41 Ktp
 Si=7.12 Qua₁₉
 Na=1.02 Jd₃₈
 Aeg₄₃ Qua₄₇
 Aeg₁₆

T=450°C	<i>experiment</i>	#57	#58	#59	#74	#76	#76	#67	#67	#66
	<i>reference</i>	6	14	16	1	2	1	22	2	7
	<i>mineral</i>	Phg	Omp	Aeg	Pl	Omp	Ttn	Omp	Ep	Phg
	P (GPa)	1.2	1.2	1.2	1.4	1.4	1.4	1.6	1.6	1.6
	SiO₂	50.96	55.14	55.02	67.84	52.57	29.29	55.77	37.74	52.89
	TiO₂	0.95	0.60	1.92	0.02	1.10	37.03	2.03	0.70	1.83
	Al₂O₃	20.29	6.29	7.82	19.97	7.91	2.67	7.89	19.68	18.15
	Fe₂O₃	-	-	-	-	-	-	-	15.75	-
	FeO	6.72	17.24	15.27	0.18	15.87	3.58	16.68	-	7.61
	MnO	0.01	0.00	0.18	0.02	0.19	0.08	0.14	0.23	0.00
	MgO	3.80	1.98	2.16	0.00	2.57	0.00	1.85	0.26	3.42
	CaO	0.00	10.34	6.07	0.00	9.84	23.88	3.91	22.79	0.00
	Na₂O	0.59	7.88	11.25	11.01	8.37	1.09	11.50	0.08	0.83
	K₂O	10.27	0.00	0.01	0.83	0.04	0.06	0.00	0.04	9.92
ΣREE	n.a.	n.a.	n.a.	n.a.	n.a.	n.a.	n.a.	n.a.	n.a.	

Total	93.59	99.49	99.71	99.87	98.46	97.68	99.77	97.27	94.64
	Si=3.56	Qua ₄₅ Jd ₃₈ Aeg ₁₇	Qua ₂₂ Jd ₃₈ Aeg ₄₀		Qua ₃₉ Jd ₃₅ Aeg ₂₆		Qua ₂₂ Jd ₄₁ Aeg ₃₆	X _{ps} =34	Si=3.65

n.a. = not analysed

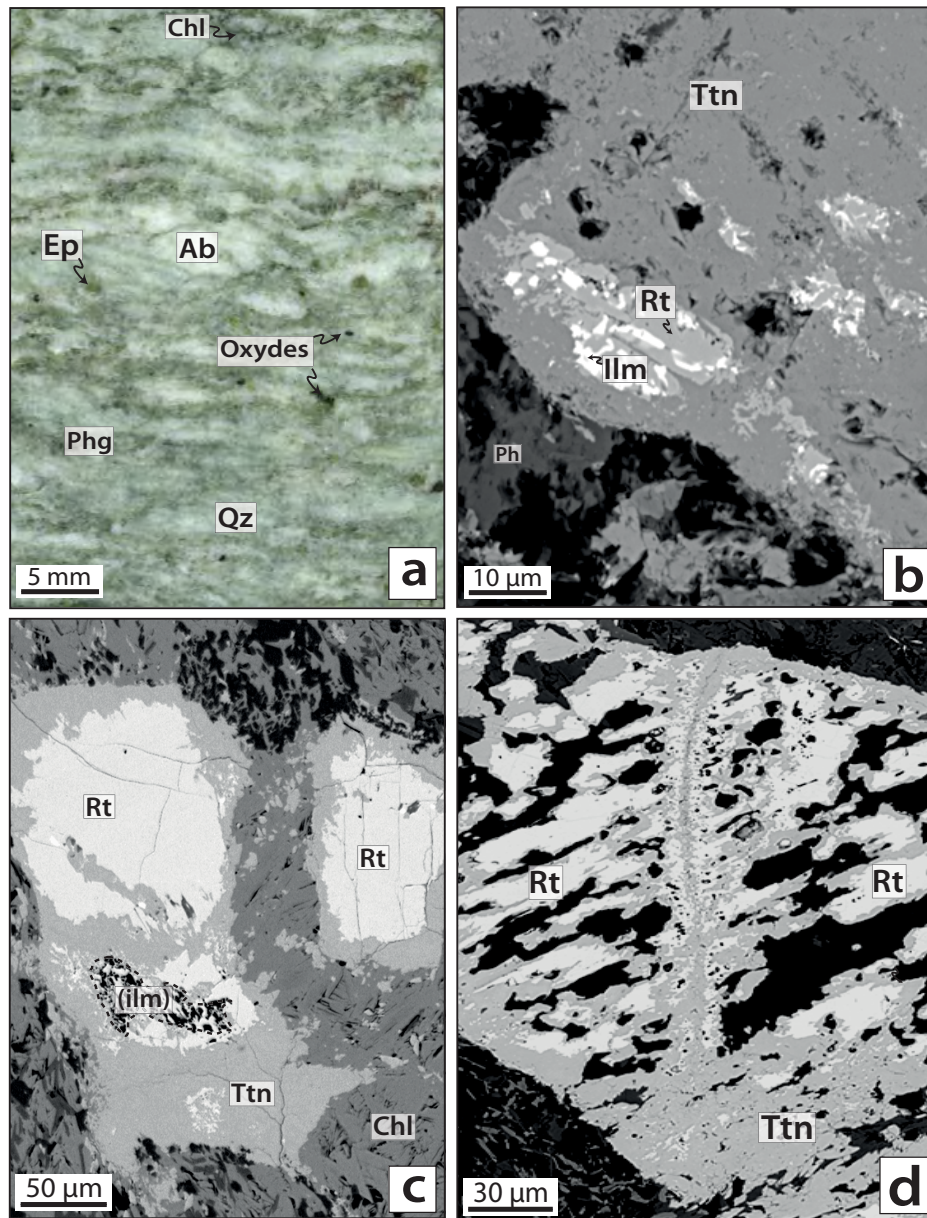


Figure 1

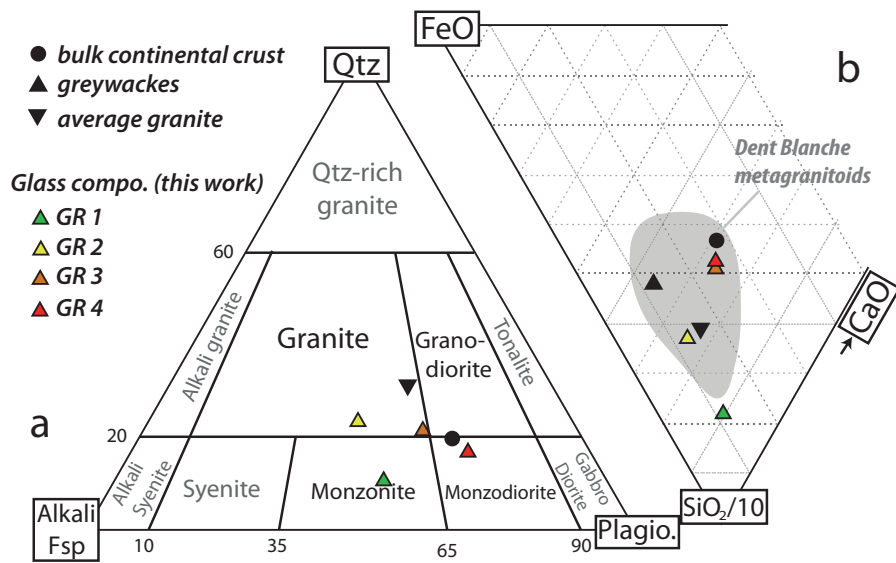


Figure 2

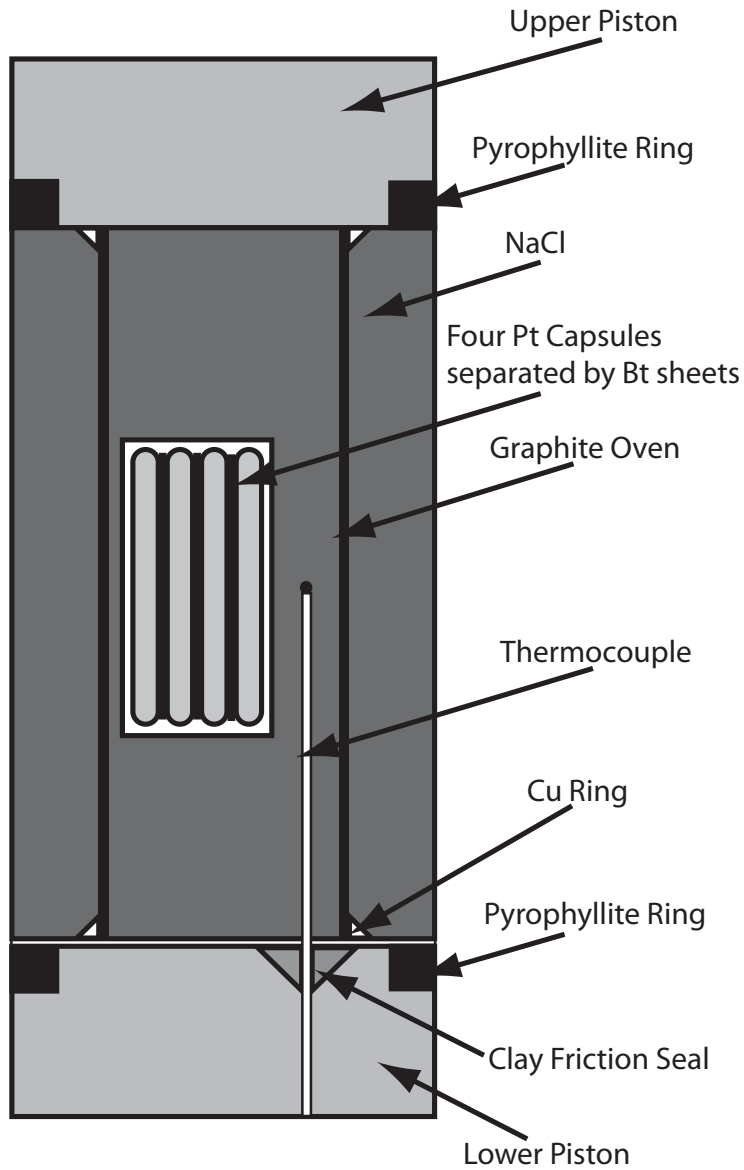


Figure 3

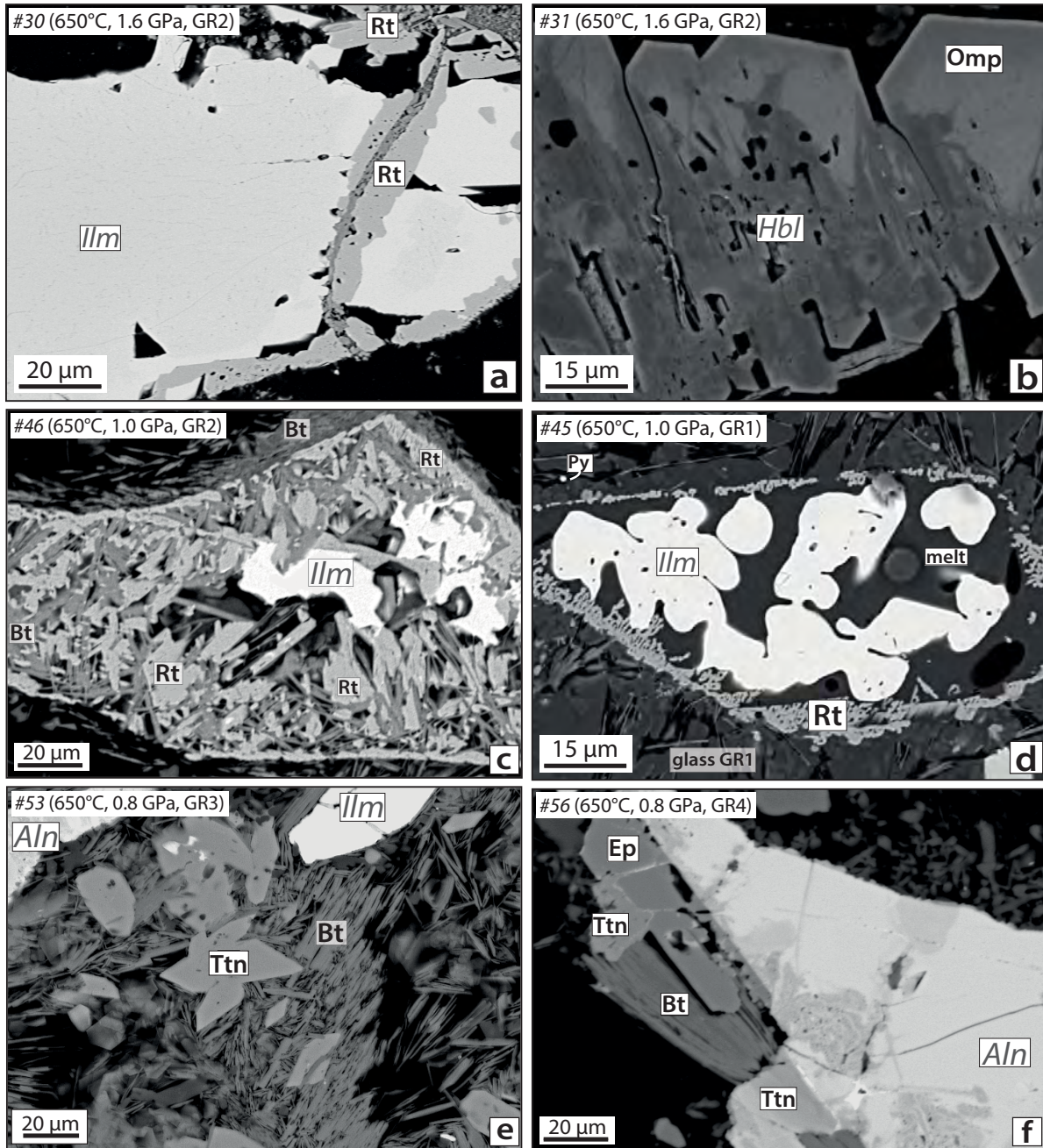


Figure 4

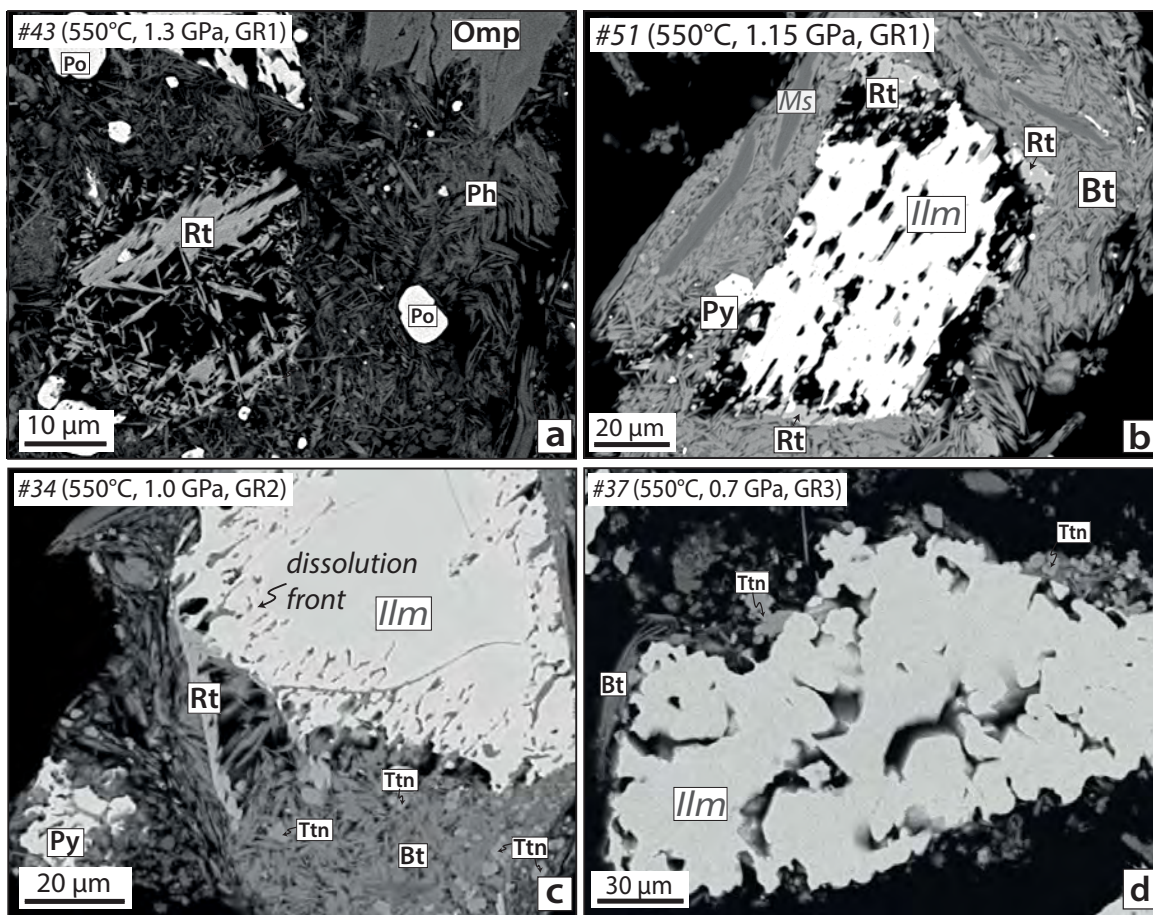


Figure 5

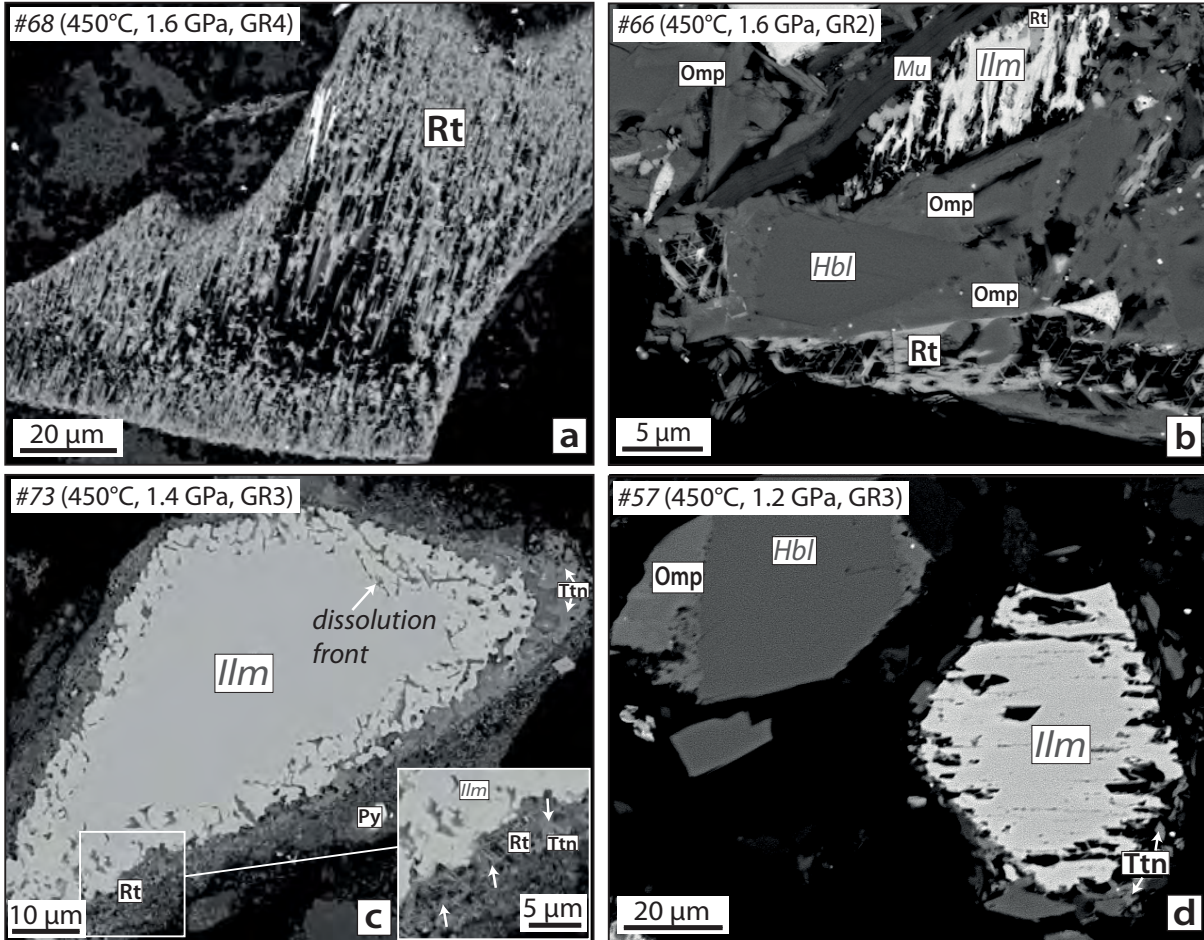


Figure 6

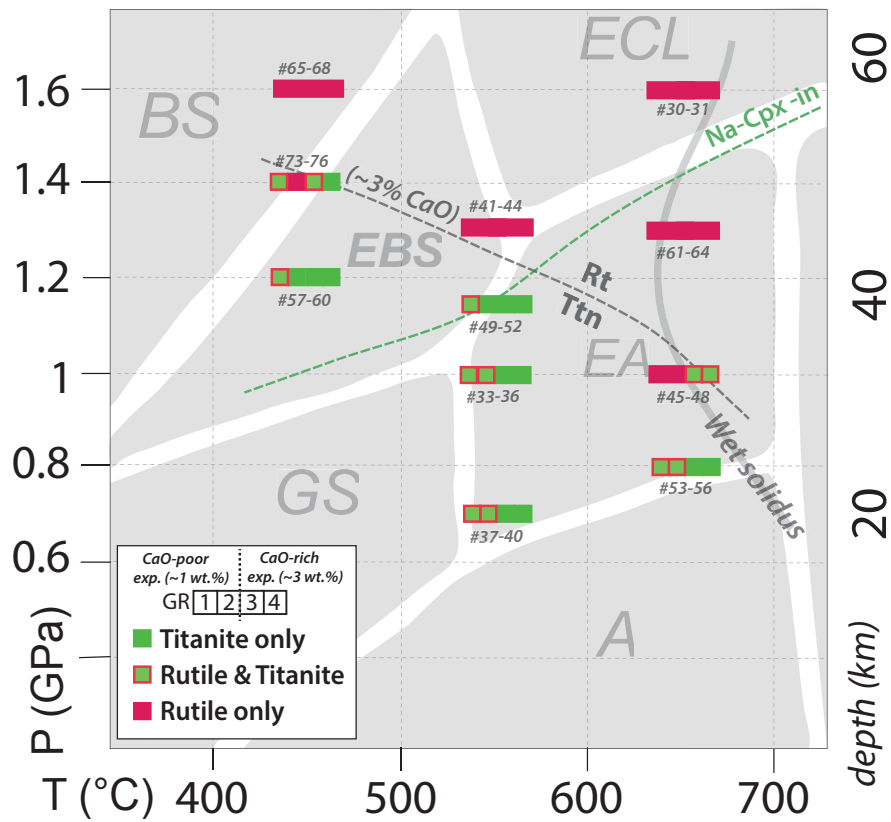


Figure 7

T = 550°C

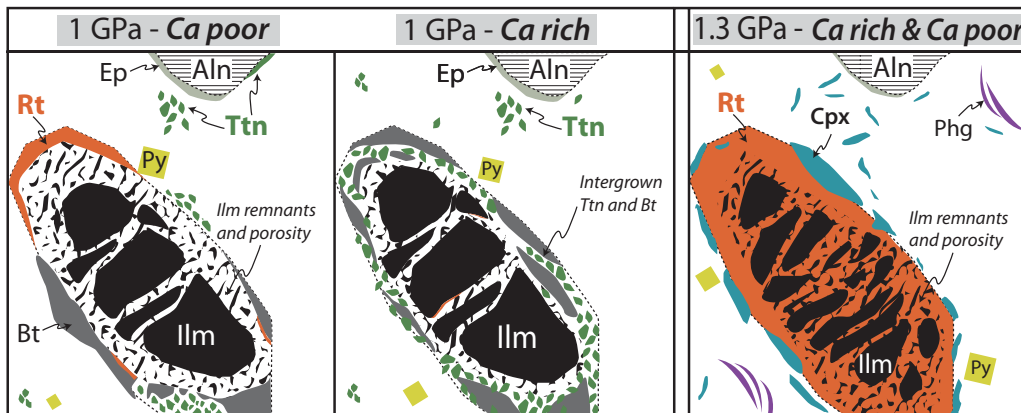


Figure 8

TABLE 1. Natural occurrences of titanite and rutile in the W. Alps

<i>Granitoid natural occurrence</i>	Peak metamorphic conditions			<i>Ref.</i>
	<i>main Ti-bearing phase</i>	<i>P (GPa)</i>	<i>T (°C)</i>	
<i>Gothard massif</i>	Titanite	0.4	400-450	[1] [2]
<i>Mont Blanc shear zone</i>	Titanite	0.5	400	[3]
<i>Mercantour granitic mylonite</i>	Titanite	0.5-0.7	350-400	[4]
<i>Suretta nappe</i>	Titanite	1	400-450	[5]
<i>Ruitor zone</i>	Titanite	1.2	450	[6] [7]
<i>Gneiss minuti</i>	Rutile	1-1.5	500-550	[8]
<i>Arolla gneiss</i>	Rutile	1.2-1.4	400-500	[9] [10]
<i>Ambin dome</i>	Rutile/Titanite	1.5	500	[11]
<i>Sesia Eclogitic Micaschist Complex</i>	Rutile	1.5-2	550	[12] [13]
<i>Sesia Eclogitic Complex orthogneiss</i>	Titanite	1.5-2	550	[14]
<i>Monte Mucrene metagranitoid (Sesia)</i>	Rutile	1.6-2	550	[15]
<i>Silvery micaschists (Gran Paradiso)</i>	Rutile	1.9-2.7	515-600	[16]
<i>Brossasco-Issasca unit (Dora Maira)</i>	Rutile	3.0-3.6	720-780	[17]

TABLE 2. Bulk rock composition of natural samples and experimental material

<i>rock type</i>	<i>meta- granitoid</i>	<i>meta- granitoid</i>	<i>meta- granitoid</i>	<i>Arolla mylonite</i>						
<i>sample ref.</i>	#54C	#67C	#67A	#34S	#05E	#34C	#35E	#12I	#35K	#17F
<i>glass ref.</i>	GR1	GR2	GR3	GR4	-	-	-	-	-	-
SiO ₂	77.50	71.70	70.30	66.21	77.43	60.40	63.00	68.90	60.10	57.90
TiO ₂	0.08	0.32	0.25	0.42	0.09	0.59	0.67	0.53	0.62	1.17
Al ₂ O ₃	11.80	13.40	14.60	15.89	12.24	18.00	16.40	13.50	16.90	15.70
Fe ₂ O ₃	0.55	2.05	1.87	2.62	1.04	3.68	3.43	2.11	2.91	1.8
FeO	0.41	1.03	0.58	0.89	n.a.	1.15	1.76	2.74	2.57	5.66
MnO	0.03	0.06	0.05	0.06	0.03	0.08	0.09	0.09	0.12	0.15
MgO	0.32	0.79	1.03	1.25	0.3	1.73	2.27	2.62	2.74	3.55
CaO	0.47	2.38	1.12	3.19	0.69	4.59	2.66	0.91	3.36	2.6
Na ₂ O	3.25	2.93	2.85	4.22	3.13	4.73	5.01	3.69	5.44	5.44
K ₂ O	4.38	3.41	5.26	2.75	4.24	1.91	1.61	1.68	1.91	0.58
P ₂ O ₅	0.02	0.08	0.07	0.12	0.02	0.18	0.25	0.15	0.19	0.22
H ₂ O	0.85	1.36	1.68	1.31	0.45	2.25	2.36	2.58	2.31	2.98
CO ₂	0.05	0.21	0.11	0.05	0.14	0.06	0.07	0.14	0.16	0.05
<i>Total</i>	99.75	99.81	99.85	98.99	99.80	99.53	99.74	99.85	99.62	98.42

TABLE 3. Composition of starting glass material and mineral seeds

	<i>glass</i>	<i>glass</i>	<i>glass</i>	<i>glass</i>	<i>Ilm</i>	<i>Hbl</i>	<i>Ms</i>	<i>Aln</i>
	GR1	GR2	GR3	GR4		starting material		
SiO₂	66.89	68.04	65.44	64.92	0.05	39.36	46.29	31.66
TiO₂	0.03	0.32	0.38	0.48	52.15	3.61	0.43	0.24
Al₂O₃	16.68	15.02	15.35	15.72	1.01	13.59	34.71	19.19
Fe₂O₃[*]	n.a.	n.a.	n.a.	n.a.	4.03	0.01	0.00	14.03
FeO	0.84	2.62	3.49	3.70	36.20	10.49	3.79	0.00
MnO	0.06	0.05	0.09	0.08	0.12	0.12	0.04	0.25
MgO	0.41	1.30	1.14	1.42	5.97	12.97	0.51	0.98
CaO	0.89	1.35	3.29	3.47	0.00	12.01	0.00	13.97
Na₂O	5.15	3.27	3.57	4.70	0.01	2.01	1.04	0.03
K₂O	6.66	5.77	4.01	3.04	0.00	2.33	8.74	ΣREE 17.90
Total	97.60	97.75	96.76	97.53	99.54	96.50	95.56	98.25

TABLE 4. Experimental conditions and starting materials (mg)

Experiment	P (GPa)	T (°C)	Time (d)	GR1 0.5% CaO	GR2 1.1% CaO	GR3 2.4% CaO	GR4 3.2% CaO	Mineral Mix	NaS	H ₂ O	Mineral products	Ti-bearing phases
#55	0.8	650	16	17.23				8.51	0.96	5.58	Bt, Ep, Fsp, Hbl, Qz, Py	Titanite, Rutile
#54	0.8	650	16		15.42			6.46	0.93	5.18	Bt, Ep, Fsp, Hbl, Qz	Titanite, Rutile
#53	0.8	650	16			13.52		5.59	0.98	5.37	Bt, Ep, Fsp, Hbl, Qz	Titanite
#56	0.8	650	16				13.74	6.96	1.17	6.13	Bt, Ep, Fsp, Hbl, Qz	Titanite
#47	1.0	650	21	12.70				6.50	1.41	5.80	Bt, Ep, Fsp, Hbl, melt, Qz, Py	Rutile
#46	1.0	650	21		14.21			6.38	1.01	4.84	Bt, Ep, Fsp, Hbl, melt, Qz, Py	Rutile
#45	1.0	650	21			14.01		6.29	0.98	4.92	Bt, Ep, Fsp, Hbl, melt, Qz, Py	Titanite, Rutile
#48	1.0	650	21				13.89	7.30	1.29	5.01	Bt, Ep, Fsp, Hbl, melt, Qz, Py	Titanite, Rutile
#63	1.3	650	20	12.88				7.09	0.97	6.08	Bt, Ep, Fsp, Hbl, melt, Qz, Po	Rutile
#62	1.3	650	20		14.30			7.57	1.10	5.78	Bt, Ep, Fsp, Hbl, melt, Qz, Po	Rutile
#61	1.3	650	20			15.85		6.59	1.32	5.63	Bt, Ep, Fsp, Hbl, melt, Qz, Py	Rutile
#64	1.3	650	20				14.97	6.66	1.30	5.41	Bt, Ep, Fsp, Hbl, melt, Qz, Po	Rutile
#31	1.6	650	21		11.60			8.70	1.10	4.70	Bt, Cpx, Ep, Qz, Py	Rutile
#30	1.6	650	21			6.90		7.70	1.20	4.90	Bt, Cpx, Ep, Qz, Py	Rutile
#39	0.7	550	21	12.84				7.22	1.26	5.76	Bt, Ep, Fsp, Qz, Po	Titanite, Rutile
#38	0.7	550	21		10.97			7.65	1.50	5.07	Bt, Ep, Fsp, Qz, Po	Titanite, Rutile
#37	0.7	550	21			11.68		5.37	1.50	3.92	Bt, Ep, Fsp, Qz, Po	Titanite
#40	0.7	550	21				14.73	6.65	1.71	5.09	Bt, Ep, Fsp, Qz, Po	Titanite
#35	1.0	550	24	17.20				6.80	0.80	5.30	Bt, Ep, Fsp, Qz, Py	Titanite, Rutile
#34	1.0	550	24		12.60			6.60	1.60	3.20	Bt, Ep, Fsp, Qz, Py	Titanite, Rutile
#33	1.0	550	24			12.90		7.00	1.60	5.00	Bt, Ep, Fsp, Qz, Po	Titanite
#36	1.0	550	24				14.60	7.70	0.70	5.40	Bt, Ep, Fsp, Qz, Py	Titanite
#51	1.15	550	21	14.57				6.76	1.27	4.97	Bt, Ep, Cpx, Qz, Po	Titanite, Rutile
#50	1.15	550	21		15.02			7.30	0.96	5.27	Bt, Ep, Fsp, Qz, Po	Titanite
#49	1.15	550	21			13.13		7.15	0.90	5.29	Br, Ep, Fsp, Qz, Po	Titanite
#52	1.15	550	21				12.51	6.40	1.30	4.89	Bt, Ep, Cpx, Qz, Po	Titanite
#43	1.3	550	21	11.97				6.69	1.86	6.14	Bt, Cpx, Phg, Ep, Qz, Po	Rutile
#42	1.3	550	21		9.86			6.69	1.61	5.62	Cpx, Phg, Ep, Qz, Py	Rutile
#41	1.3	550	21			12.45		6.60	1.02	4.97	Cpx, Phg, Ep, Qz, Po	Rutile
#44	1.3	550	21				13.45	7.20	1.48	5.48	Cpx, Phg, Ep, Qz, Py	Rutile
#59	1.2	450	42	13.45				6.79	1.41	4.86	Cpx, Phg, Ep, Qz, Py	Titanite, Rutile
#58	1.2	450	42		12.53			7.30	1.20	5.13	Cpx, Phg, Ep, Qz, Py	Titanite
#57	1.2	450	42			14.03		7.42	0.73	5.56	Cpx, Phg, Amp, Ep, Ab, Qz, Py	Titanite
#60	1.2	450	42				15.00	8.23	0.95	5.41	Cpx, Phg, Chl, Ep, Qz, Py	Titanite
#75	1.4	450	11	11.63				7.99	0.97	5.59	Cpx, Phg, Qz, Py	Titanite, Rutile
#74	1.4	450	11		12.56			7.54	1.67	5.50	Cpx, Qtz, Fsp, Bt, Qz, Po/Py	Rutile
#73	1.4	450	11			14.20		7.06	0.82	5.03	Cpx, Phg, Ep, Qz, Py	Titanite, Rutile
#76	1.4	450	11				12.97	5.39	2.39	5.53	Cpx, Fsp, Qz, Po	Titanite
#67	1.6	450	56	15.76				7.17	0.64	5.81	Cpx, Phg, Ep, Qz, Py	Rutile
#66	1.6	450	56		15.05			6.68	1.27	5.73	Cpx, Phg, Ep, Qz, Py	Rutile
#65	1.6	450	56			12.64		8.76	1.46	4.97	Cpx, Phg, Ep, Qz, Py	Rutile
#68	1.6	450	56				15.85	6.59	1.32	5.63	Cpx, Phg, Ep, Qz, Py	Rutile

TABLE 5. Composition of experimental products

<i>experiment</i>	#45	#45	#47	#47	#62	#61	#64	#64	#31	#31
<i>reference</i>	6	10	21	4	1	3	10	12	69	2
<i>mineral</i>	<i>Ttn</i>	<i>melt</i>	<i>melt</i>	<i>Ttn</i>	<i>Ttn</i>	<i>Ep</i>	<i>Bt</i>	<i>Hbl</i>	<i>Rt</i>	<i>Aeg</i>
T=650°C	<i>P (GPa)</i>	1.0	1.0	1.0	1.0	1.3	1.3	1.3	1.6	1.6
	SiO₂	30.31	67.46	69.93	27.58	30.57	38.97	38.42	42.92	52.62
	TiO₂	36.97	0.47	0.52	35.01	37.86	0.86	2.65	1.50	95.94
	Al₂O₃	0.84	13.01	13.31	1.39	1.69	24.63	15.70	13.21	0.15
	Fe₂O₃	-	-	-	-	-	10.12	-	-	-
	FeO	1.38	0.88	0.70	1.45	1.51	0.00	17.57	17.09	3.41
	MnO	0.01	0.02	0.01	0.06	0.00	0.23	0.11	0.26	0.00
	MgO	0.00	0.05	0.03	0.23	0.00	0.02	10.63	7.87	0.00
	CaO	28.15	0.53	0.42	25.78	27.94	23.18	0.00	8.90	0.03
	Na₂O	0.09	4.30	1.69	0.16	0.00	0.00	0.31	4.01	0.18
	K₂O	0.10	2.59	3.11	n.a.	0.00	0.00	8.90	0.93	0.02
	ΣREE	n.a.	n.a.	n.a.	1.12	n.a.	n.a.	n.a.	n.a.	n.a.
	Total	97.85	89.31	89.73	92.78	99.57	98.01	94.30	96.69	99.44
							X _{ps} =21	X _{Mg} =0.52	Si=6.49	Na=1.18
										Qua ₃₁
										Jd ₁₉
										Aeg ₅₀
	<i>experiment</i>	#39	#34	#34	#51	#44	#43	#44	#43	#43
	<i>reference</i>	54	1	2	82	32	50	52	42	47
	<i>mineral</i>	<i>Rt</i>	<i>Ttn</i>	<i>Bt</i>	<i>Bt</i>	<i>Ep</i>	<i>Phg</i>	<i>Amp</i>	<i>Aeg</i>	<i>Omp</i>
T=550°C	<i>P (GPa)</i>	0.7	1.0	1.0	1.15	1.3	1.3	1.3	1.3	1.3
	SiO₂	0.22	30.04	39.25	38.95	37.72	49.30	46.87	54.55	54.78
	TiO₂	94.94	35.12	2.50	3.69	1.31	1.72	0.60	2.39	1.50
	Al₂O₃	0.06	1.90	16.97	12.83	23.46	20.59	9.33	7.81	7.40
	Fe₂O₃	-	-	-	-	11.79	-	-	-	-
	FeO	2.72	1.45	19.36	21.25	0.00	9.81	18.87	15.47	8.52
	MnO	0.01	0.05	0.13	0.16	0.21	0.05	0.24	0.11	0.31
	MgO	0.01	0.00	7.35	7.95	0.14	4.40	7.90	2.40	7.18
	CaO	0.06	27.30	0.04	0.00	22.56	0.00	5.45	4.43	10.72
	Na₂O	0.10	0.12	0.40	0.25	0.09	0.25	5.39	11.68	7.60
	K₂O	0.05	0.24	9.12	9.35	0.03	9.78	0.44	0.02	0.26
	ΣREE	n.a.	n.a.	n.a.	n.a.	n.a.	n.a.	n.a.	n.a.	n.a.
	Total	97.98	96.22	95.12	94.43	97.31	95.90	95.10	98.86	98.26
								Ktp	Qua ₁₉	Qua ₄₇
						X _{ps} =24	Si=3.41	Si=7.12	Jd ₃₈	Jd ₃₅
								Na=1.02	Aeg ₄₃	Aeg ₁₆
	<i>experiment</i>	#57	#58	#59	#74	#76	#76	#67	#67	#66
	<i>reference</i>	6	14	16	1	2	1	22	2	7
	<i>mineral</i>	<i>Phg</i>	<i>Omp</i>	<i>Aeg</i>	<i>Pl</i>	<i>Omp</i>	<i>Ttn</i>	<i>Omp</i>	<i>Ep</i>	<i>Phg</i>
T=450°C	<i>P (GPa)</i>	1.2	1.2	1.2	1.4	1.4	1.4	1.6	1.6	1.6
	SiO₂	50.96	55.14	55.02	67.84	52.57	29.29	55.77	37.74	52.89
	TiO₂	0.95	0.60	1.92	0.02	1.10	37.03	2.03	0.70	1.83
	Al₂O₃	20.29	6.29	7.82	19.97	7.91	2.67	7.89	19.68	18.15
	Fe₂O₃	-	-	-	-	-	-	-	15.75	-
	FeO	6.72	17.24	15.27	0.18	15.87	3.58	16.68	-	7.61
	MnO	0.01	0.00	0.18	0.02	0.19	0.08	0.14	0.23	0.00
	MgO	3.80	1.98	2.16	0.00	2.57	0.00	1.85	0.26	3.42
	CaO	0.00	10.34	6.07	0.00	9.84	23.88	3.91	22.79	0.00
	Na₂O	0.59	7.88	11.25	11.01	8.37	1.09	11.50	0.08	0.83
	K₂O	10.27	0.00	0.01	0.83	0.04	0.06	0.00	0.04	9.92
	ΣREE	n.a.	n.a.	n.a.	n.a.	n.a.	n.a.	n.a.	n.a.	n.a.
	Total	93.59	99.49	99.71	99.87	98.46	97.68	99.77	97.27	94.64

	Qua ₄₅	Qua ₂₂	Qua ₃₉	Qua ₂₂		
Si=3.56	Jd ₃₈	Jd ₃₈	Jd ₃₅	Jd ₄₁	X _{ps} =34	Si=3.65
	Aeg ₁₇	Aeg ₄₀	Aeg ₂₆	Aeg ₃₆		

n.a. = not analysed